Numerical Analysis of an Axial Flow Horizontal Axis Marine Hydrokinetic Turbine

Aarshana Parekh

A thesis

submitted in partial fulfillment of the

requirements for the degree of

Master of Science

University of Washington

2019

Committee:

Alberto Aliseda, Chair

James Riley

Dana Dabiri

Program Authorized to Offer Degree:

Mechanical Engineering

University of Washington

Abstract

Numerical Analysis of an Axial Flow Horizontal Axis Marine Hydrokinetic Turbine

Aarshana Rajeev Parekh

Chair of the Supervisory Committee:
Prof. Alberto Aliseda
Mechanical Engineering

:

Tidal energy extraction using marine hydrokinetic devices has become an important area of research in the renewable energy field in recent years because of the highly predictable nature of the tides. Due to its early stage of development many studies need yet to be done before deployment of these devices at tidal sites. It is essential to have a thorough understanding of the turbine performance and wake properties before determining the array arrangement for tidal farms. In this thesis, flow behavior in the wake of a counter-rotating dual rotor horizontal axis tidal turbine is studied by numerically solving the Reynolds Averaged Navier Stokes (RANS) Equations. The rotational effects of the turbine are modeled using the sliding mesh technique. The realizable $k-\varepsilon$ model is employed to solve the closure problem. The methodology is validated against experimental data measured in open channel tests conducted at the St. Anthony Falls Laboratory of the University of Minnesota, in collaboration with Sandia National Laboratory, to investigate the turbine efficiency and the physical dynamics of the wake. The transient performance of the turbine is predicted with good accuracy using the sliding mesh model, with some level of disagreement found in predicting the velocity deficit in the flow. The limitations of accurately predicting the turbulent flow properties for the turbine are addressed and the sliding mesh

technique is proven to capture effectively the different coherent structures in the wake. The qualitative agreement of the method suggests that this model can be used to explore turbine design and wake characteristics over various parameters in a cost-effective manner. This method can also provide critical parameters needed for designing efficient tidal farms.

TABLE OF CONTENTS

LIST OF FIGURES

LIST OF TABLES

ACKNOWLEDGEMENTS

I would like to thank my advisor, Prof. Alberto Aliseda whose unyielding support, encouragement, and supervision from the beginning to the end helped me complete this project . I would also like to thank Prof. Brian Polagye, Prof. James Riley and Prof. Dana Dabiri for teaching me about tidal energy and turbulence modeling. They provided me with invaluable knowledge and helped me gain a deeper understanding of the fundamentals required in this project. This work would not have been possible without the support from SAFL at the University of Minnesota, Sandia National Laboratory as well as the faculty and staff members of the University of Washington Mechanical Engineering Department. Last but not the least, in am forever grateful to my family and friends for their unwavering support and for constantly encouraging me to surpass myself.

DEDICATION

To my parents and sister, thank you for always having faith in me

To my grandparents, thank you for your blessings and constant support

Chapter 1. INTRODUCTION

Over the past few decades, to cater to the increasing energy demand along with reducing greenhouse emissions, the United States of America and the European Union have set goals for producing energy from renewable resources and increasing energy efficiency. For example, the Energy Policy for Europe was put forward in 2014 to address issues like energy supply, climate change, and industrial development. One of the critical goals of this policy is to have a 27% share of renewables in overall energy consumption for the EU by 2030[1]. The state of Washington, in the year 2006, passed Initiative 937, which requires utility companies to generate 15% of all electricity consumed by the state from renewable resources like solar, wind, tidal, and upgrading existing hydropower plants (excluding new hydropower facilities) by 2020 [2].

Alongside these political policies, engineers and researchers are working on either maximizing the efficiency of existing technologies used for harnessing power from renewable resources or investigating alternative forms of energy sources to supply the ever-increasing demand for electricity and other types of energy like mechanical energy. Tidal energy is one such source of energy which is still in its research and development phase as opposed to wind or solar power, which have developed technology for commercial use. The idea behind tidal power is to extract potential energy in the form of kinetic energy produced by the surge of ocean waters during the rise and fall of tides.

Tides are a periodic motion of waters in the sea due to gravitational forces between the Sun, Moon, and Earth. According to Newton's law of gravitation, there exists a force of attraction between two bodies with different masses, m_1 and m_2, with a distance r between them that acts along the line intersecting the masses. This force is directly proportional to the product of the two masses and inversely proportional to the square of the distance between them:

$$F_{12} = F_{21} = G\frac{m_1 m_2}{r^2} \tag{1.1}$$

Where F_{12} and F_{21} are the attractive forces, and G is the universal gravitational constant with the value of $6.6743\times10^{-11}\left[N(kg/m)^2\right]$. As the orientation of the Earth and Moon changes with respect to the Sun, this force of attraction changes the height of sea and ocean water lever[3], [4]. When the Sun and Moon are in line with the Earth, their gravitational forces are added together to

produce the strongest tide, known as the spring tides. On the contrary, when the Sun and Moon are in opposite positions with respect to the Earth, the resultant gravitational forces act against each other to produce the weakest tide called neap tides, as seen Figure 1.1

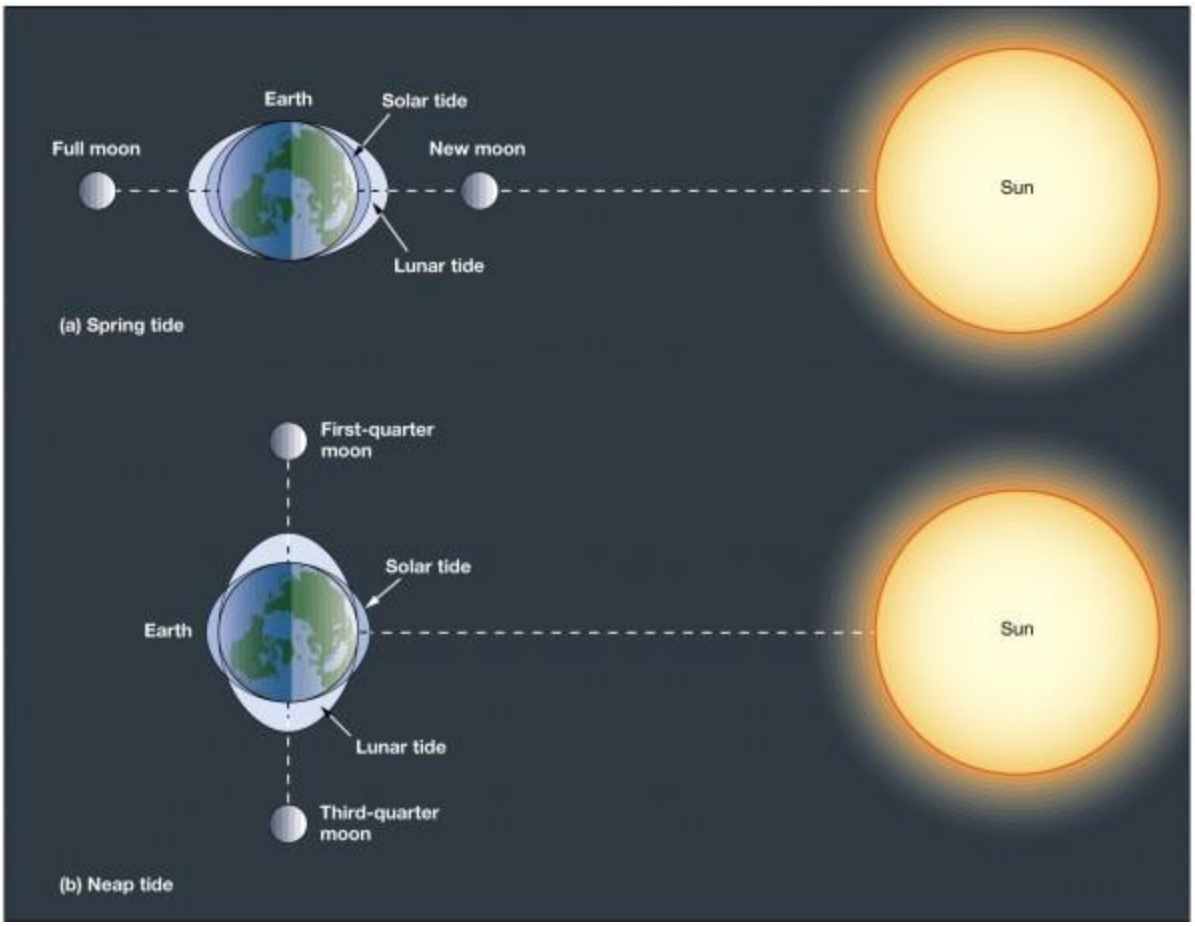

Figure 1.1:Schematic of spring and neap tides formation based on Sun, Moon, and Earth positions[5].

Though the principle of tide formation is due to the Sun and the Moon, the Moon is the main tide generating body. Because of a greater distance, the Sun's effect on the tide magnitude is only 30% [4].

1.1 METHODS FOR TIDAL ENERGY GENERATION

There are two kinds of devices used for generating electricity by harnessing energy from the tides: tidal range devices and tidal stream generators[6]. The tidal range devices generate electricity by utilizing the difference in water level between high and low tides, while the tidal stream devices capture the kinetic energy of flowing water to generate electric power.

1.1.1 *Tidal Range Devices*

Tidal range devices can be classified into two types: tidal barrages and tidal lagoons. A tidal barrage is a device that uses a large dam called a barrage which is constructed across tidal rivers, bays, and estuaries. The turbines inside the barrage harness tidal power, similar to how river dams harness the power of a river. As the tides rise, the barrage gates are opened, and at high tide, the gates are closed. This action creates a head difference as the water recedes to a low tide level. The water is then released through the hydroelectric turbines stored in the barrage which extract energy from the flowing water as depicted in Figure 1.1. The most well-known barrage system is 220MW Rance River Tidal Power Station in Brittany, France, which was commissioned in 1966 and has been running on full capacity since 1968 [7]. There are currently only three locations using tidal barrages to extract power due to the high installation costs and environmental impacts associated with this technology [8].

A tidal lagoon is a body of ocean water partly enclosed by a naturally or artificially constructed barrier. The lagoons might also be estuaries or freshwater reservoirs. Tidal lagoons function similar to tidal barrages; however, unlike barrages, they can be built along the coastline and generate continuous power. The turbines generate electricity as the lagoon is filling and emptying. Fundamentally compared to barrages, the environmental impact of tidal lagoons should be minimal as they can be constructed by natural materials like rock and would act as low seawall during low tide but be submerged at high tide. Hence animals could swim around the walls, and smaller life forms could swim inside it. Due to the low water level difference, the energy output from the generators is less than that of barrages. Currently, there are no working examples that have succeeded in implementing this method to support the idea of tidal lagoon. Though, the Chinese government has commissioned a 300MW tidal lagoon powerplant project near the mouth of the Yalu River [9].

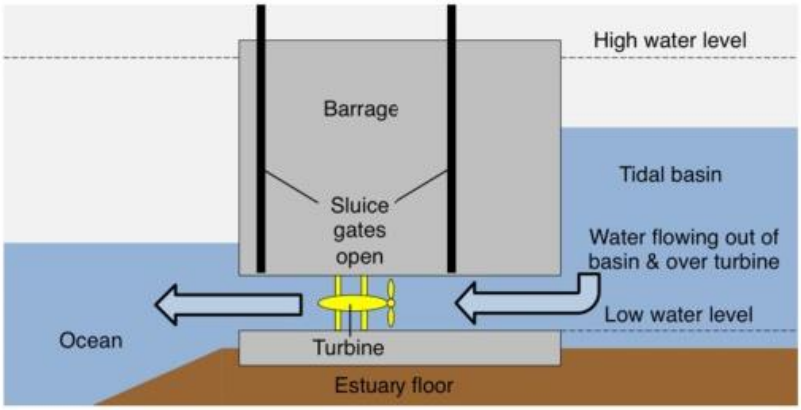

Figure 1.2: Tidal barrage [6]

1.1.2 *Tidal Stream Devices*

Tidal currents occur in conjunction with the rise and fall of tides. They are created due to the horizontal motion of water caused because of the vertical motion of tides near the shore. As the current moves towards the land it "floods" and when it recedes back to the sea it "ebbs". Tidal currents are affected by the Earth, Moon, and Sun orientation like the tides resulting in strong currents in regions with flows driven through narrow passages by high water elevation. These flows contain a significant amount of kinetic energy. Tidal stream devices exploit this kinetic energy to generate tidal power. The specific flux of kinetic energy in these flows is defined as:

$$P = \frac{1}{2}\rho A V^3 \tag{1.2}$$

Where ρ is the density of seawater, A is the cross-sectional area that the current goes through and V is the velocity of the flow. Tidal stream devices extract energy from water in a manner similar to that of a wind turbine harnessing wind energy. Though one must note that, compared to winds that travel at average speeds of 12 m/s, tides flow at relatively low velocities (approximately 2-3 m/s) but have significantly higher energy conversion potential as water is ~1000 times denser than air [9]. The flow around a wind turbine is unconstrained and incompressible with a maximum coefficient of power of 0.593. This is known as the Betz limit and was derived using the stream tube analysis of flow around the turbine also called the Linear Momentum Theory - Actuator Disk Model [10]. The coefficient of power is defined as:

$$C_p = \frac{P_t}{\frac{1}{2}\rho A_d U_\infty^{\,3}} \tag{1.3}$$

Where P_t is the power generated by the turbine, ρ is the density of the fluid, A_d is the area of the turbine, and U_∞ is the free stream velocity. For unconstrained flows, tidal stream generators, also known as marine hydrokinetic (MHK) turbines, have a very low blockage ratio and the Betz limit can apply as the flow conditions are similar to wind turbines. However, in most cases, the bathymetry of tidal energy sites and the presence of free surface effects means that the Betz limit can no longer be applied, making it possible to have power coefficients above 59% [11].

According to Garret [11], the maximum power is given by:

$$P_{\max} = \frac{16}{27}\left(1-\varepsilon\right)^{-2}\frac{1}{2}\rho A_d U_\infty^{\,3} \tag{1.4}$$

Where ε is the blockage ratio defined as the ratio of the area of the turbine (A_d) to the cross-sectional area of the flow and U_∞ is the free stream velocity of the flow. The new term $\left(1-\varepsilon\right)^{-2}$ is due to constrained flow conditions. The above relation is derived by conducting a one-dimensional analysis between two rigid surfaces. Thus, it only considers the increase in blockage ratio and not the change in free surface height resulting from energy extracted by the turbine.

Polagye [12] performed a similar analysis but took into account the free surface effects and also investigated the influence of the mixing region on turbine performance. According to this study the power harnessed depends on the blockage ratio, the channel's Froude number (Fr) defined in eq(1.5), and the ratio between inlet velocity and velocity downstream of the turbine.

$$Fr = \frac{U}{\sqrt{gl}} \tag{1.5}$$

In the equation: U is the flow speed, g is gravitational acceleration, and l is the characteristic length scale. Another major difference between wind and tidal power is that tidal energy is a highly predictable source. The low and high tides develop with well-known cycles which make it easier to design a system with accurate dimensions since the operating conditions that the equipment is subjected to are known a priori.

Unlike wind energy, tidal energy technology is still in its development stage leading to various types of turbine configurations being offered by different companies. The most prominent arrangements implemented are the vertical and horizontal axis turbines. The axis of rotation for a

vertical axis or a crossflow turbine is perpendicular to the free stream flow while that for axial flow turbines is parallel to the direction of flow. There are several types of blade designs used for vertical axis turbines (VAT), but the two significant configurations are the straight blade classic Darrieus turbine and the helical blade-shaped turbine seen in Figure 1.3. The helical shaped blades are subjected to almost constant loading as opposed to the Darrieus turbine, which leads to the increased lifespan of the machine [13]. A benefit of using crossflow turbines is that they are well suited for use in turbine farms since they can be placed very close to each other like the Ocean Renewable Power Company's TidGen 150 kW crossflow tidal gravity foundation configuration, seen in. If stacked in a tower, the tidal farm only requires one generator, which reduces the cost of the project [14].

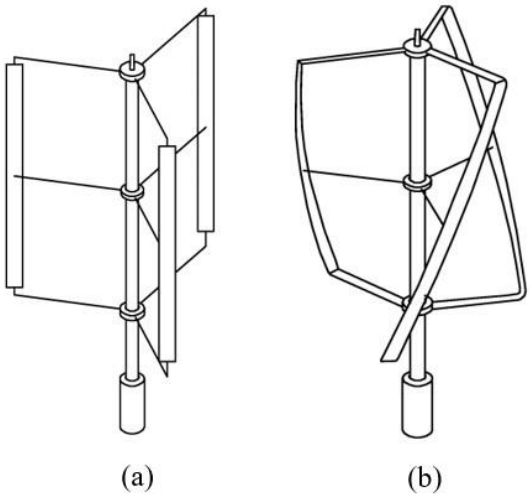

Figure 1.3: Cross Flow turbine configurations (a) H – Darrieus Type (b) Helical Type. Source [15]

Horizontal axis tidal turbines (HATT) have the same working principle and similar energy conversion as their wind turbine counterparts. The turbine blades are composed of 2D hydrofoil cross-section blades and extract energy based on the lift generated by the hydrofoil. The airfoil is subjected to a resultant force arising from the inflow velocity and angular velocity of the rotor. This force has the lift and drag components acting in the plane of the rotor, normal to the turbine axis. The net torque produced due to the lift and drag forces is transferred via the shaft to the gearbox to the alternator. These turbines are subjected to higher loads as the density of water is much larger than the density of air. The possibility of cavitation coupled with the wear and tear of the support structure results in a design much stockier and bulkier than wind turbines.

For this project, however, we are interested in the HATTs as compared to VATs as HATTs are much more efficient with peak performance achieved at higher rotor speeds [14]. Another advantage of horizontal axial turbines is that they are self-starting as the lift forces are generated evenly over the blade. Another reason for selecting this configuration is that previous studies on HATTs can be used to validate the results. Due to extensive literature available on turbine design and performance information, the accuracy of the simulations can be evaluated with these results as well as those provided by the experimental data.

Currently, there exist multiple proposed designs that employ this configuration such as the Verdant Power and Marine Current Turbine's models as shown in Figure 1.4. Verdant Power, from 2006 to 2009, tested six full-scale prototypes in the East River in New York City, making them the first commercially certified array of tidal turbines [from]. They used a three-blade axial flow open tip configuration with a monopile foundation. The Marine Current Turbine's (MCT) SeaGen device was the world's first commercial-scale tidal generator as seen in Figure 1.4. The design has a dual rotor tidal monopile foundation with a unique horizontal support arm that can be raised to allow servicing of turbine above water. For this project, we study the performance of a horizontal axis turbine with a configuration similar to that of the SeaGen device consisting of two dual bladed counter rotors with a monopile foundation and horizontal support arms.

1.2 THESIS OUTLINE

Chapter 2, Literature Review and motivations, provides an overview of the current search available for HATT, especially emphasizing the various numerical methodologies used to analyze turbine performance. Chapter 3, Methodology, describes the methodology along with the numerical simulation settings and model parameters used in thesis. Chapter 4, Results and Discussion focusses on the analysis of the results obtained through the simulations and their validation with experimental data. Chapter 5, Conclusions and Future Work provides a summary of the thesis and highlights the critical conclusions.

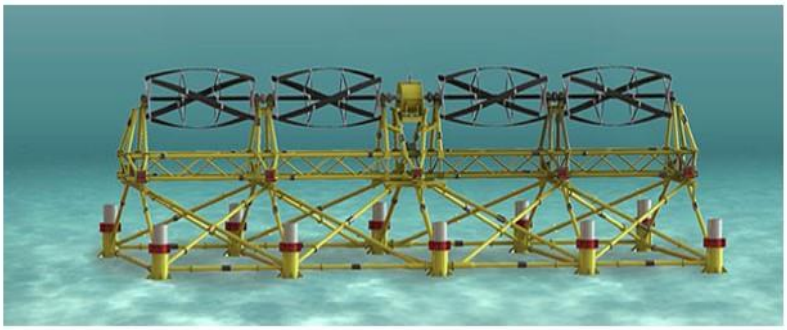

(a) TidGen 150 kW crossflow gravity foundation

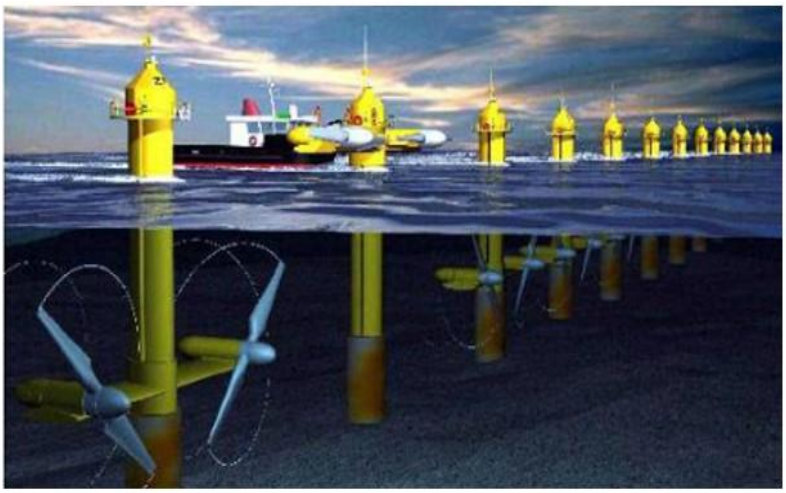

(b) Marine Current Turbine's SeaGen 1.2MW

(c) Verdant Power Tidal turbine configuration

Figure 1.4: Tidal turbine devices from leading companies. Source: company website

Chapter 2. BACKGROUND

2.1 MOTIVATION

Over the past decades, the necessity to balance the ever-increasing need for energy and to conserve the conventional sources of energy (fossil fuels) has ignited the demand for alternative sources of energy generation. Due to its predictability, low environmental impact, and no necessity of large civil works structures, compared to dams, tidal energy is an attractive alternative to hydropower take advantage of the potential energy in the world's rivers and estuaries. This has led to the increased research efforts on tidal energy converters in recent years with a spike in interest in understanding the hydrodynamics of these devices. Many designs and configurations have been tested, as mentioned in Chapter 1, with one of the most common arrangements being the horizontal axis tidal turbine. As highlighted earlier, there are many similarities between wind and tidal turbines. However, compared to wind energy, which is a mature technology with over forty years of intense research, tidal energy is a relatively new technology and still in the research and development phase. Due to its short time in the public eye in the modern era, there is limited data published, and hence there are still gaps in our understanding and modeling capabilities of flow around such devices.

Due to the difficulty in performing full-scale measurements of the turbines in their natural environment, numerical modeling provides an opportunity to analyze the turbine design as well as to predict environmental effects before deployment, with low costs and short turn-around times. The goal of this thesis is to develop a numerical methodology to simulate the performance of a dual turbine, counter-rotating rotor, HATT. With this model, we hope to gain insight into the flow dynamics around and in the wake of the turbine. These will provide quantitative information on the performance and environment effects, respectively, of an isolated HATT, and serve as a foundation for study of large turbine arrays.

Analysis of the wake plays a crucial role in determining the inter-device spacing and layout of turbine arrays. The fluid passing through the turbine rotor experiences a reduction in velocity across the rotor plane. The length, width, and persistence of the wake are vital factors that must be considered while designing tidal farms. Placed too close, the devices would suffer from a decrease in performance while placing them too far would result in sub-optimal use of surface area within

the regions of strong tidal flow, limited in the worlds estuaries and constricted channels by the very nature of the resource (the power is proportional to the cubic power of the flow velocity, and thus only regions where the velocity is high are efficient and economically viable for deployment of HATTs). The aim for this thesis is, through numerical simulations, to understand the structure and dynamics of the fluid downstream of the turbine, near and mid-field wake, as well as to gather information on the influence of flow parameters on the wake propagation and recovery. We hope that the data collected can be useful in designing an optimal tidal farm for this dual-rotor HATT configuration. Along with the validation through comparison of the numerical prediction of performance to the experimental measurements, we also aim to establish on solid ground what are the limitations of numerical simulations, using a moving mesh approach to the rotor geometry and a turbulence model for closure of the RANS equations, in this application. In this context, we used the data gathered from the open channel experiments conducted at the St. Anthony Falls Laboratory, Minnesota, in collaboration with by Sandia National Laboratories, testing a scaled-down version of Department of Energy's Reference Model 1 HATT.

2.2 LITERATURE REVIEW

Horizontal axis tidal turbines have been a subject of interest for researchers in the past few years as a result of increasing demand for tidal energy extraction technologies. Several studies have been conducted both experimentally and numerical to understand the hydrodynamics and estimate the performance of these turbines. There have been very few full-scale experimental tests performed on MHK turbines and none in the public domain, due to the difficulties of deploying the turbine in strong tidal currents. Hence much of the analysis available on the open literature to date is done with scale down versions of the turbine model. One of the first experiments on HATT was conducted by Bahaj et al. [16] using a $1/16^{th}$ scaled model of a three-bladed marine current device (MCT) with a rotor diameter of 800 mm. Tests were conducted in a 2.4 m ×1.2 m cavitation tunnel and a 60 m towing tank to calculate the power and thrust coefficients for a range of tip speed ratios (TSRs) and blade pitch angles. The results obtained through this study provided information on the operation of single turbines in straight or yawed flow, the effect of performance changes in tip immersion of the rotor, and insight on likely areas of cavitation inception. It also produced a set of

consistent experimental data that was useful in the validation of numerical methods and simulation models developed in the future.

Numerical simulations are a beneficial and comparatively inexpensive alternative to experimental analysis to understand the turbine dynamics and performance but require validation to ensure accurate capture of the physics. There are many methodologies developed to model MHK turbines, but in general, there are two ways used to simulate flow around turbines, namely the virtual disk method and blade resolved method. The first approach is a simplified technique in which the effect of the rotating blade on the surrounding flow is modeled. The blade geometry is not resolved in this technique, and the body forces acting on the turbine are distributed over a cylindrical disk volume. The easiest way to implement this approach on turbines is through Actuator Disk Model (ADM). ADM is based on the one-dimensional stream tube analysis of the flow [10]. Here the body forces on the flow are distributed along the swept area of the turbine given by:

$$A = \pi R^2 \tag{2.1}$$

Where R is the radius of the turbine rotor. While conducting lab experiments using this approach, the turbine is represented as a porous disc with a diameter equal to that of the rotor. This porous media applies force to the surrounding flow, similar to the thrust of the turbine. Myers and Bahaj [9] conducted experiments using static disc mesh simulators with a diameter of 100 mm to understand the downstream wake structure recovery of free stream velocity profile for a HATT. The resistance offered by the disc was transferred to the flow as thrust force. The thrust coefficient was varied by changing the disc porosity. It was found that hole size and frequency also influence the thrust characteristics. For discs with equal porosity, smaller and a more significant number of holes would result in higher thrust as compared to fewer larger holes. The cause of this behavior was attributed to increasing orifice losses due to decrease in hole diameter. For numerical simulations the disc is created by assigning a region in the fluid domain as a porous zone with cross sectional area equal to the turbine rotor. This porous media is depicted by the source term in the momentum equations.

Harrison et al. [17] conducted a comparative study between numerical simulations and experiments for predicting the far wake of HATT using the ADM. The tests were conducted in a water channel measuring 21m in length, 1.37 m in width and a water depth of 0.3m. Multiple discs of diameter 0.1m with varied porosity and different materials were used to change the thrust force acting on the discs. The different materials resulted in different near wake flow characteristics. For

the numerical simulations, the turbine was modeled using a cylindrical porous zone with the same diameter as the experiments and a thickness of 0.001 m. Experimental thrust values were matched in the simulations by varying the resistance coefficient of the porous zone. Results show that the turbulence in the near wake is underpredicted causing the far wake to recover at a slower rate.

The ADM approach is computationally less expensive as compared to modeling a full turbine[3], [17]. The shorter computation time is partially due to the model working in steady-state and partly due to the mesh resolution[17]. Since a simplified geometry of a disc is used to represent the rotor blades, phenomena like boundary layer and flow separation are not recorded [13]. Also, the disc extracts energy from the flow by converting stream-wise momentum to small scale turbulence structures that dissipate quickly behind the disc. This type of turbulence is an effect of the porous nature of the disc and not a realistic approximation of that produced by the rotating turbine blades [17]. Since the disc is not rotating, some of the flow physics is not captured. For example, the swirl induced in the flow and the tip vortices shed by the rotating blades[17].

Since the ADM approach has shown to underpredict the velocity deficit in the far wake and inaccurately capture the near wake characteristics [3] models were developed which capture more of the physics of the turbine blades. Two such models used to model marine and wind turbines are the Blade Element Momentum Theory (BEMT) model and Blade Element Model (BEM). The BEMT model is based on a combination of the blade element theory (BET) and the linear momentum theory (LMT). The LMT is used to derive the axial and circumferential induction factors. A tip loss factor is also introduced to account for the finite number of rotor blades. The BET is used to calculate the lift and drag forces of the blade. In this method, the rotor blade is divided into multiple sections from root to tip. The lift and drag forces for each section are derived based on the angle of attack (AOA), chord length, airfoil type. Lift and drag coefficients of each element. The thrust and power coefficients are calculated by the integration of these forces over the entire blade [18]. The BEM is a numerical model used to simulate the effects of the rotating blade on the surrounding fluid by using a momentum source term. In this method, like the ADM, the turbine is modeled as a disc fluid zone with the cross-section area equal to the rotor swept area. The momentum source term is based on the body forces (lift and drag) in the x, y and z directions acting inside the fluid disc. The model uses BET to calculate the body forces which are averaged over a full turbine rotation. The source term is calculated for each cell in the disc zone, and the

flow is updated with these forces[3]. Turnock [19], Batten [20], Malki[21] and Javaherchi [3] have successfully applied the BEMT model and the BEM to MHK turbines.

Bahaj [18] validated two models based on the BEMT, which were based on the codes used for wind turbines but were modified to suitably represent the new marine technologies. These codes included a blockage correction since they were incapable of modeling confinement effects. The lift and drag coefficient data for the BET were derived using a 2-D airfoil performance code, XFoil. Xfoil is a linear vorticity stream function panel method which has a viscous boundary layer solution that acts via surface transportation model. The power and thrust performance of both models, when compared with the experimental data, showed that one code underpredicted the thrust, and the other overestimated the power. They stipulated that the reasons for these discrepancies were due to errors in the blockage corrections applied to the experimental data.

Batten [20] adapted a numerical program based on the BEM theory for wind turbines developed by Barnsley and Wellicome[15]. The model included significant enhancement to deal with operation in water and pressure increase due to wake. The lift and drag data for each element were derived using the 2D panel code XFoil. The numerical model was validated by comparing power and thrust coefficients with data from the experiments conducted by Bahaj [16], Batten et al. [20] observed good agreement between the two sets of results and mentioned that this validated method could be used for designing and optimizing energy output with tidal data.

Turnock el at [19] used the coupled Reynolds Averaged Navier Stokes (RANS) -BEMT approach to model tidal turbine wakes for analyzing power capture of arrays of turbines. The coupled BEMT approach commonly used to study array optimization of wind turbines employed the BEMT code Cwind modified for tidal turbines validated by experimental results similar to Batten [20]. The total power produced by the array was found to be dependent on the longitudinal and lateral spacing of the turbines with the optimal power potential achieved with a small lateral spacing and large longitudinal spacing.

Like the ADM approach, the BEM model does not explicitly model individual turbine blades, and therefore has shorter run times and relatively quick achievement of convergence [21]. Thus, has lower computational demands. However, this approach does not resolve all of the details directly downstream of the turbine, and the tip vortices are not properly captured, making it only suitable for studies involving information only for the far wake [3]. A disadvantage of the BEM model is that the coefficients of lift and drag for the blade must be known beforehand to predict the

performance. Since both ADM and BEM approaches are steady-state models the transient effects are disregarded, and the instantaneous flow characteristics and performance cannot be calculated [4].

An alternative approach to the simplified models is conducting simulations of a fully resolved turbine model to deal with the rotating effect of the blades. The two techniques commonly applied to achieve this motion are the frozen rotor approach, also known as the Moving Reference Frame (MRF) model, and the Sliding Moving Mesh (SMM) model [22]. The MRF model renders the unsteady problem around the blade into a steady-state problem. In this method the effect of rotation is input into the fluid equations of motion by body forces that represent the inertial effects associated with the centrifugal and Coriolis accelerations [3]. This enables solver to integrate the equations in a stationary grid, thereby avoiding the complexity of stiffness associated with the SMM model simulation [23]. The downside of this approach is that it requires an axisymmetric domain and periodic boundary conditions[23].

In this thesis our focus is on the SMM model, where like the MRF model the effects of the rotating blades on the fluid domain are simulated by using a highly detailed computational mesh around individual turbine blades, with the physical no-slip condition on the blade surface. The domain is divided into rotating and stationary subdomains but unlike the MRF model this technique is unsteady and is used to compute full three-dimensional Reynolds Averaged Navier Stokes (RANS) equations in the channel and around the turbine. At each time step, the inner region encasing the turbine rotates with respect to the outer domain. Over the last decade many studies have successfully employed this technique to conduct transient analysis of wind and tidal turbines to gain more insight into the turbine performance and wake behavior.

Sun and Zhang in 2010 [24] conducted numerical simulations to predict the performance of a phase VI Horizontal axis wind turbine (HAWT) with a rotor diameter of 10 in an unsteady airflow field. The turbine was given a rotational speed of 72rpm, the effects of which are modeled using the sliding mesh technique. User-defined functions were used to control the mesh motion. The rotor torque and surface pressure coefficient distribution at 30% and 80% spanwise locations predicted by the numerical simulations were compared with experimental data from the NREL UAE wind tunnel test to validate the model. Upon examination, it was found that the numerical results were in good agreement with the experimental data. Sun et al. [24] concluded that the sliding mesh technique is a feasible method used to predict the aerodynamic performance of a HAWT.

McNaughton et al. [25] and Afghan et al. [26] implemented a new methodology for sliding meshes to perform three-dimensional simulations which predict mean and unsteady behavior of the wakes and power production for a wall- and blade- resolved laboratory-scale three-bladed HATT. The accuracy of the numerical simulations was assessed by direct comparison to published experimental data [16]. Both studies applied this methodology to simulate the MHK turbine using RANS models and LES. All turbulence models produced the thrust and power coefficients as a function of TSR with optimal values at TSR = 6, matching the experimental results. In both studies, the LES method produces better agreement between the simulation and experimental data over a wider range of TSR but is computationally expensive. While the RANS models show allowable agreement and produced acceptable results at lower computation costs.

Leroux et. al [27]performed three-dimensional numerical simulations of a three-bladed HATT under realistic turbulent tidal flow conditions. The sliding mesh model was used to model the effect of turbine rotation on the flow. The Reynolds Averaged Navier Stokes (RANS) Shear Stress Transport (SST) k – omega model was used to cater the turbulence closure problem for the simulations. The analysis was conducted over a range of tip speed ratios (TSR = 3-4.5) and flow velocities (1.6, 1.8, 2.05 m/s) at a fixed hub pitch angle of 28°. Results for thrust and power coefficients predicted by the transient simulations were validated by comparing with data obtained from steady flow simulations. When examined for both models showcase similar trends for C_p and C_t curves. However, an approximate 4% reduction in performance (for TSR = 3.5) was observed in the transient simulations. It was stipulated that the increased uncertainty was due to levels of scattering in the numerical data points.

Liu et al. [22] studied flow characteristics of the wake of a horizontal axis turbine with a rotor diameter of 20 m and a blade profile of the NACA 683-xx series. The rotating effect of the blade was modeled using the sliding mesh model for transient analysis and the MRF approach for quasi-steady analysis. The results obtained were compared with theoretical and experimental data (Batten et al. [20]). On comparison, it was found that the sliding can more accurately predict the turbine performance from the wake and currents as compared to the MRF method. The model accurately estimates the transient characteristics of the wake.

Recently, Leroux et al. [28] performed a computational fluid dynamics study on the same three-bladed HATT using both quasi-steady and transient approaches with the aim to predict wake produced by the turbine as well as turbine performance. The Moving Reference

Frame(MRF)/frozen rotor approach and sliding mesh model were used for the quasi-steady and transient analysis respectively. The accuracy of the results predicted by the numerical simulations was measured by comparing them with experimental data recorded by the French Research Institute for Exploration of the Sea (IFREMER). Both numerical approaches in-cooperated the RANS SST $k-\omega$ turbulence closure model. Simulations over a range of tip speed ratios (TSR = 0.5 – 8) and a constant incoming velocity of 0.8 m/s were carried out. The power and thrust coefficients obtained from the simulations show good agreement with the experiments. Comparison of the wake captured at TSR = 3.67 by both numerical approaches and experiments shows that -the MRF method is computationally less expensive could be used to rapidly determine the turbine thrust and power coefficients (performance indicators). However for a better understanding of the wake behavior the transient approach using the sliding mesh should be employed. The main drawback of the sliding mesh model approach is that the method has higher computational costs relative to the ADM and BEMT due to the transient solution, calculation of boundary layer flow on the blades and a complicated discretized domain. The model, however, does not require tabulated coefficients of lift and drag or empirical correction factors like the BEM approach. One of the main objectives of this thesis is to gain deep understanding of fluid behavior in the near and far wake regions downstream of the turbine. As mentioned earlier, while ADM and BEM are computationally less expensive and accurately predict the far wake behavior, they do not record the near wake characteristics well[23]. For capturing the near wake, the turbine model must be three-dimensionally resolved. The sliding mesh approach is proven to perform better than the quasi-steady MRF method in accurately predicting the turbine performance and wake behavior in transient conditions[22], [28]. Thus, for this study the sliding mesh model was selected to simulate the rotating effects of the blade on the flow.

To conclude the literature review, we see that while there is extensive work carried out on the wake characteristics of horizontal axis wind turbines very little information is available on the wake of MHK turbines. Though there are few studies conducted related to three-bladed single rotor HATTs there is not much information on the flow properties surrounding the dual rotor HATT configuration considered for this thesis. In order to use this configuration in tidal farms in the future in-depth knowledge of the turbine wake's structure both in the near and far wake region as well as its transient nature is essential. The three-dimensional steady-state and transient analysis of HATT mentioned in this literature highlight that for an in-depth understanding of the wake and

accurate capture of the helical vortices a three-dimensional sliding mesh approach is necessary. This is the methodology developed and employed in this thesis, further information on which is provided in the next chapter.

Chapter 3. METHODOLOGY

Over the past few decades, Computational Fluid Dynamics (CFD), has become a powerful tool for physical understanding and modeling of the simplest to the most complex problems in fluid mechanics. It is an important tool for solving non-linear and turbulent flows like marine energy, complementing, and expanding the range of problems that can be tackled by experimental analysis. The CFD solver used for this thesis is StarCCM++ (CCD-Adapco/Siemens, Melville, NY). StarCCM+ is a finite volume solver, and its algorithm consists of three key steps; integration of governing equations of fluid flow over all the control volumes of the domain, discretization of these integral equations into algebraic equations, and solving the equations using an iterative method.

In this chapter, a detailed explanation of the numerical methodology used to simulate the flow around marine hydrokinetic turbines is provided. The first section of this chapter describes the governing equations, turbulence closure model, and sliding mesh technique used to simulate the flow around the turbine. Next, we characterize the domain geometry, including near-wall modeling, and the mesh generation for the simulations. The last part of this chapter covers the boundary conditions and simulation physics used for evaluation.

3.1 GOVERNING EQUATIONS

The governing equations used for this thesis to calculate the mean flow variables of each discretized fluid domain element are the Reynolds Averaged Navier Stokes (RANS) equations. The RANS equations are derived by Reynolds decomposition of each solution variable ϕ into its mean or averaged value $\bar{\phi}$ and fluctuation components ϕ'.

$$\phi = \bar{\phi} + \phi' \tag{3.1}$$

Where ϕ represents the velocity components, pressure, energy, or species concentration. The ensemble-averaging process is applied to calculate the mean values as the conditions for the flow are transient. On inserting the decomposed solution variables into the Navier Stokes equations, we get the equations of mass, momentum, and energy transport for the average quantities.

These equations are written as follows:

$$\frac{\partial \rho}{\partial t} + \nabla \bullet (\rho \bar{\mathbf{v}}) = 0 \tag{3.2}$$

$$. \frac{\partial}{\partial t}(\rho \bar{\mathbf{v}}) + \nabla \bullet (\rho \bar{\mathbf{v}} \otimes \bar{\mathbf{v}}) = -\nabla \bullet \bar{p}\mathbf{I} + \nabla \bullet (\bar{\mathbf{T}} + \mathbf{T}_{RANS}) + \mathbf{f}_b \,. \tag{3.3}$$

Where ρ is the density, $\bar{\mathbf{v}}$ is the mean velocity, $\bar{p}$ is the mean pressure, $\mathbf{I}$ is the identity tensor, $\bar{\mathbf{T}}$ is the mean viscous stress tensor, and $\mathbf{f}_b$ is the resultant body forces. Compared to the Navier Stokes equations, the above equations have an additional term in the momentum and energy transport equations. This term is known as the Reynolds stress tensor and is defined as in eq (3.4)

$$\mathbf{T}_{RANS} = -\rho \begin{pmatrix} \overline{u'u'} & \overline{u'v'} & \overline{u'w'} \\ \overline{u'v'} & \overline{v'v'} & \overline{v'w'} \\ \overline{u'w'} & \overline{v'w'} & \overline{w'w'} \end{pmatrix} + \frac{2}{3} k \rho \mathbf{I} \tag{3.4}$$

Here k is the turbulent kinetic energy. The Reynolds stress tensor creates nine (six due to symmetry) unknown terms in the mean flow equations. These terms form a closure problem and require turbulence closure models to solve this system of equations.

3.2 Turbulence Closure Models

The closure problem mentioned in the previous sections presents a challenge to model the Reynolds stresses in terms of the averaged flow quantities, which has led to the rise in the development of a myriad of turbulence modeling methods that can be used to solve this problem. One widely used approach is based on the principle of turbulent eddy viscosity μ_t based on the analogy between the molecular gradient diffusion process and turbulent motion. The standard method used to model the stress tensor is known as the Boussinesq approximation, as shown in eq(3.5).

$$\mathbf{T}_{RANS} = 2\mu_t \mathbf{S} - \frac{2}{3}(\mu_t \nabla \cdot \bar{\mathbf{v}})\mathbf{I} \tag{3.5}$$

Where **S** is the mean strain tensor given by eq (1.7)

$$\mathbf{S} = \frac{1}{2}(\nabla \bar{\mathbf{v}} + \nabla \bar{\mathbf{v}}^T) \tag{3.6}$$

Two of the most popular eddy-viscosity models used for prediction of flow around a HAT are the $k-\varepsilon$ and the Shear Stress Transport (SST) $k-\omega$ models [17], [19], [22]. The SST $k-\omega$ model developed by Menter [29] is a modified $k-\omega$ model that uses the. $k-\omega$ .formulation to model the near-wall region and used the standard $k-\varepsilon$ model to predict the flow after it transitions away from the wall. It is a commonly accepted method for modeling flow around wind and tidal turbines[4], but it has shown to underpredict eddy-viscosity in the wake and the wake recovery rate [30]. When used for transient analysis using wind turbines, this method has performed poorly in predicting the normalized power predictions by as much as 50%. The turbulence in the wake of the turbine is anisotropic and studies have shown that the SST $k-\omega$ model cannot accurately capture this anisotropy [31] and that the $k-\varepsilon$ model is better suited for predicting this phenomenon [22]. The $k-\varepsilon$ model also underestimates the strength of the three-dimensional structures compared to the other RANS models. Hence in this research, the realizable $k-\varepsilon$ two-layer variant of this approach, provided by Simcenter StarCCM+ is employed. The standard $k-\varepsilon$ model first developed by Jones and Lauder [32] has shown to accurately predict free shear flows but faces difficulty in modeling separation, wall-bounded flows, and high-pressure gradients [4]. Another downside of this method is the stiffness associated with the equations when integrated through the viscous sublayer. The realizable $k-\varepsilon$ takes into account the blocking effects of the wall, i.e., the viscous and buffer layer and, thus, is used to model flows at low-Reynolds number, as compared to the standard $k-\varepsilon$ model. The realizable k-epsilon model by Shih [33], contains a new transport equation for the turbulent dissipation rate ε and the critical coefficient C_μ expressed as a function of the mean flow and turbulence properties. The idea of variable C_μ enables the model to define the Reynolds stresses compatible with the physics of turbulence since this concept is consistent with experimental observations in boundary layers. In the two-layer approach formulated by Rodi [34], the computation is divided into two segments. In the first layer, next to the wall, turbulent dissipation rate and turbulent viscosity μ_t are calculated as functions of wall distance. This dissipation rate is blended smoothly with the values computed by solving the transport equation in the region far away from the wall. Next, the equation for k is solved the entire domain. Compared to the low Reynolds number approach where we use damping functions to modulate coefficients ($C_\mu, C_{\varepsilon 1}$ and $C_{\varepsilon 2}$) of the original model [32] as functions of turbulence Reynolds number, the results

obtained through the two-layer method are better [35], even though the calculation of ε and μ_t is equally empirical. By combining the two-layer approach with the realizable k-epsilon model, we can use it along both wall functions $(y^+ > 30)$ and near-wall modeling $(y^+ \sim 1)$ meshes. These changes to the standard $k-\varepsilon$ enable the modified technique to show a superior ability to capture the mean flow of complex structures and, for flows involving rotation and boundary layers under strong adverse pressure gradients, separation, and re-circulation. The constant values for the $k-\varepsilon$ model used to simulate flow around the MHK turbine are summarized in Table 3.1. These parameters were applied with no changes to the default parameter settings provided by Simcenter StarCCM+

Table 3.1: Constant values for k-epsilon turbulence model

Realizable k-epsilon Two-layer Model						
C_M	C_t	$C_{\varepsilon 1}$	$C_{\varepsilon 2}$	C_μ	σ_ε	σ_k
2	1	1.44	1.9	0.09	1.2	1

3.3 NEAR WALL MODELLING (WALL Y+)

After the selection of the turbulence closure model, the next step is a representation of the near-wall region. Walls are a source of vorticity and hence have a significant influence on most fluid flow applications, especially high shear imposing no-slip wall boundaries. A decrease in tangential velocity fluctuations due to viscous damping and reduction in normal velocity fluctuations due to kinematic blocking is observed very close to the wall. However, in the outer part of the near-wall region, there is a rapid increase in turbulence due to the turbulent kinetic energy produced due to sizable mean velocity gradients [36]. This region is not only an essential source or vorticity and turbulence but also has an impact on the mean flow characteristics. Hence, it is crucial to have an accurate prediction of the flow across the boundary layer to analyze wall-bounded flows.

As shown in Figure 3.1 Three zones in the near-wall region. Source [38] the near-wall region is made up of three main zones; first is the viscous sublayer, then the buffer layer or blending zone, and lastly, the fully turbulent or log-law region. The viscous sublayer is the zone nearest to the wall. The flow in this zone is essentially laminar, with Reynolds stresses negligible compared to

viscous stress. The mean flow velocity depends on fluid density, viscosity, wall distance, and the wall shear stress. The log law region is the outer region where the direct effects of viscosity on the flow velocity are negligible and are dominated by turbulence effects[10]. The non-dimensional wall distance y^+ defined by eq (3.7) is applied to calculate the extent of each layer.

$$y^+ = \frac{\rho y u_*}{\mu} \tag{3.7}$$

Where y is the wall distance, ρ is the density of the fluid, μ is the dynamic viscosity of the fluid and u_* is the friction velocity:

$$u_* = \sqrt{\frac{\tau_\omega}{\rho}} \tag{3.8}$$

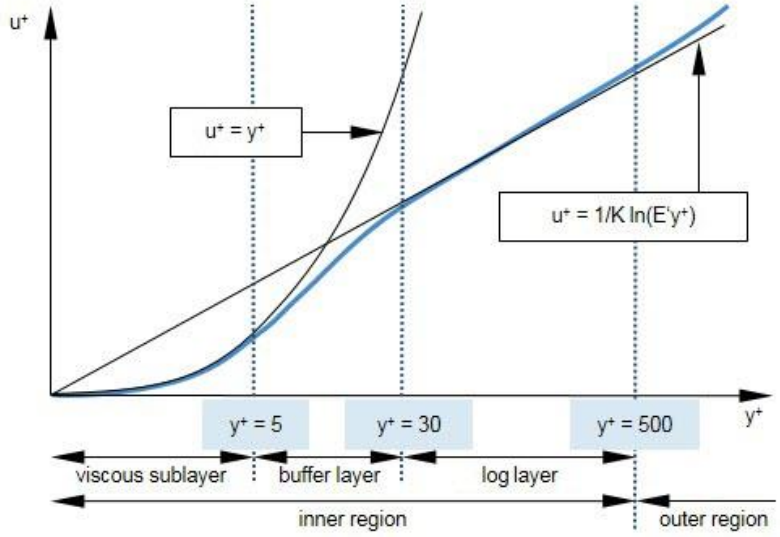

Figure 3.1 Three zones in the near-wall region. Source [38]

Modeling of the near-wall can be achieved using three different approaches:

- High y^+ or wall function approach:

  This method uses assumed distributions of velocity and turbulence quantities across the boundary to provide boundary conditions for the RANS equations. The accuracy of this method depends on the extent to which these approximations agree with the reality of the application. The viscosity-affected region in the viscous sublayer and buffer layer are analytically modeled in this method, and the wall functions are based on the log-law of the wall, as shown in Figure 3.2. The first cell near the wall must be within the log layer of the

boundary ($y^+ > 30$). The main advantage of this treatment is less computation time due to lower number of near-wall cells.

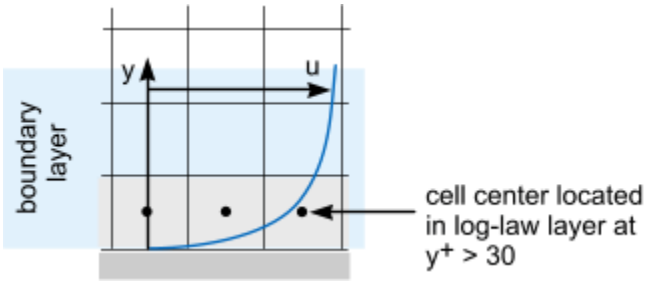

Figure 3.2: Wall Function Approach. Source [38]

- Low y^+ or near-wall modeling approach

  The boundary layer in this method is modeled using a thin-layered mesh with near-wall cells located at $y^+ \sim 1$ with the viscous sublayer wholly resolved as observed in Figure 3.3. As compared to the wall function approach, this treatment is computationally more expensive. This is especially for flows with high Reynolds number (Re), as viscous sublayer physical dimensions are in micron or submicron scales, and any problem of industrial or environmental significance requires millions to billions of cells to resolve. Hence this approach is suitable for relatively low Re flows.

- All y^+ wall treatment approach

  This treatment uses blended wall functions that imitate low y^+ for fine meshes and high y^+ for coarse meshes. This method is used when the wall cell centroid falls within the buffer zone of the boundary layer hence is suitable for a range of mesh densities as depicted in Figure 3.3.

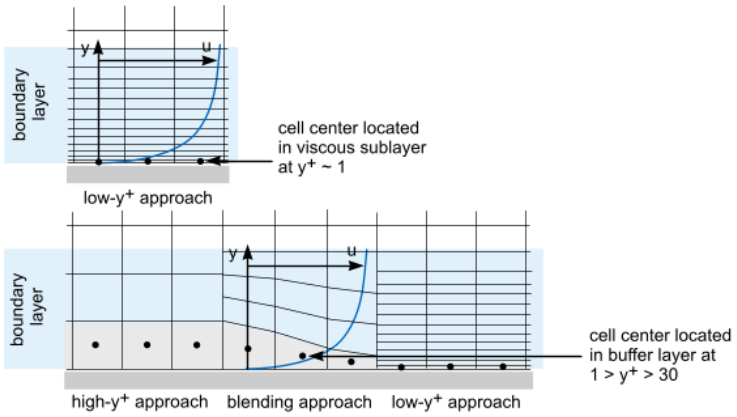

Figure 3.3: Low y^+ and All y^+ wall modeling approaches. Source [38]

The simulations for this research occur at Reynolds number of approximately 3×10^5, a relatively low Reynolds number flow, and to simulate the flow along the rotating wall of the turbine blades, the viscous sublayer must be resolved[4]. Hence the low y^+ wall treatment is considered to capture the boundary layer dynamics.

3.4 MESH MOTION

In order to simulate the rotating motion of the turbines, the sliding mesh technique is employed. The channel domain is divided into three regions. The outer stationary region and two inner cylindrical rotating areas. The two rotating zones include the counter-rotating rotors of the turbines, which move at a specified rate with each time step. The outer stationary zone comprises the rectangular channel, the turbine hub, horizontal and vertical support arms surround the two rotating regions, as shown in Figure 3.4. The rotating and stationary zones meet at the mesh interface along which they are coupled to each other. The arrows highlight the direction of flow through the channel.

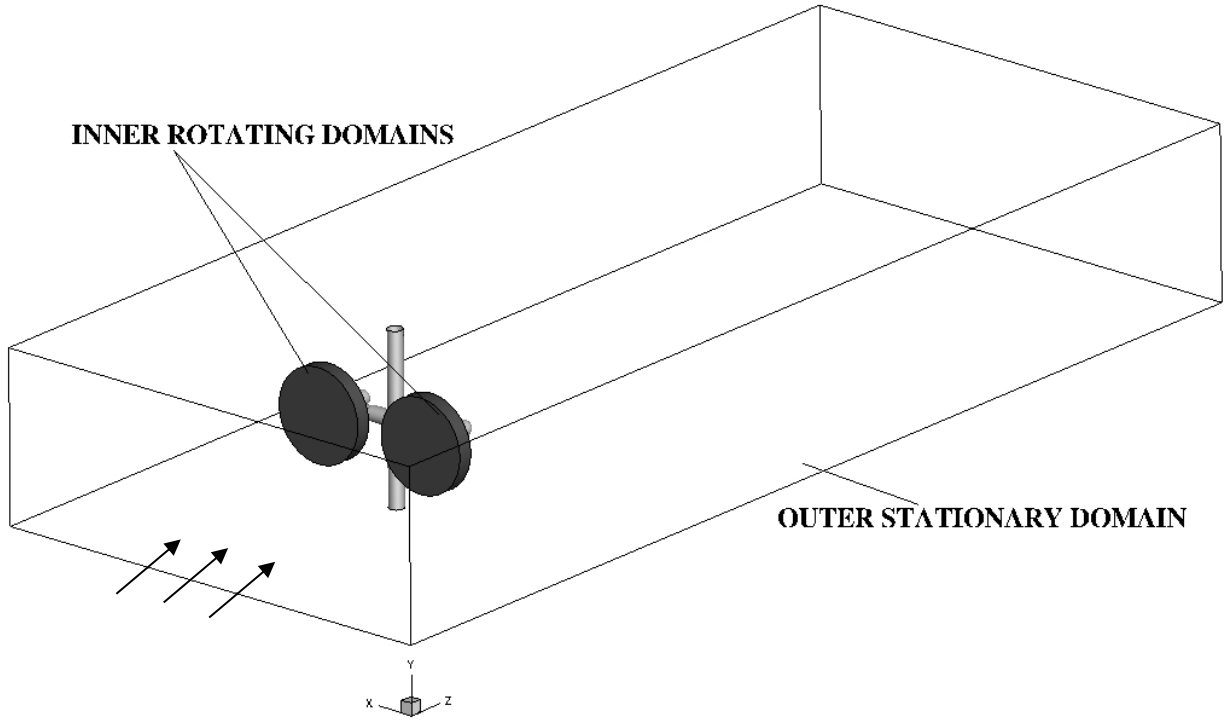

Figure 3.4: Rotating and stationary domains

Mesh motion modifies the flow conservation equations due to the addition of flux in the convective terms. The flow equations for dynamic meshes with a moving reference frame are given as follows:

Conservation of mass:

$$\frac{\delta}{\delta t}\int_V \rho dV + \oint_A \rho(\mathbf{v}_r - \mathbf{v}_g)\cdot d\mathbf{a} = \int_V S_u dV \tag{3.9}$$

Conservation of momentum:

$$\frac{\delta}{\delta t}\int_V \rho\mathbf{v}dV + \oint_A \rho\mathbf{v}\otimes(\mathbf{v}_r - \mathbf{v}_g)\cdot d\mathbf{a} = \oint_A \sigma\cdot d\mathbf{a} + \int_V f_b dV - \int_V \rho\omega\times\mathbf{v}dV \tag{3.10}$$

Where $\mathbf{v}_g$ is the grid velocity or mesh velocity in the laboratory reference frame, S_u is the source term, σ is the stress tensor, f_b are the body forces and $\mathbf{v}_r$ is the relative velocity defined by the moving reference frame. The use of a moving reference frame is no longer required as the rotating motion is defined with respect to the laboratory/stationary reference frame, which simplifies the flux calculations across the interface. The fictitious force (the last term in eq. (3.10)) arising from the non-inertial frame reference frame vanishes as $\mathbf{v}_r = \mathbf{v}$,i.e. velocity for stationary meshes. For

sliding meshes, the position of the cells in the rotating region varies with time but the control volume remains constant.

The grid velocity for the sliding mesh in this thesis is defined in eq (3.11)

$$\mathbf{v}_g = \omega_g \times r \tag{3.11}$$

Where ω_g is the prescribed angular velocity of the mesh and r is the position vector of the mesh vertex. This approach is comparatively more accurate that the moving reference method but is more computationally demanding due to the unsteady flow field [22]. One disadvantage of using the sliding mesh technique is that the rotating regions are subtracted from the stationary domain. The only way to ensure that the separate domains are aware of the changes on the other side is by updating values at the interface. It is essential to update the values at the interface at every time step.

A direct interface is used to connect the two boundaries of the neighboring grid for each time step. StarCCM+ has several direct interface types available and, for this work, an internal interface is employed. When included in the meshing process, Simcenter StarCCM+ forms a conformal boundary across the interface surfaces wherever applicable and, if the faces are non-conformal, a new discretization is created. The connection between cells on each side of the interface is made to ensure the transport of mass and/or heat transfer flux across the intersected area at each time step. For the current application, an in-place interface topology has been used as it does not have any periodic or repeating interface and the two regions do not have any physical separation in space between them. Figure 3.6 shows an example of the in-place interface used in the domain. The value or flux of any variable at the control volume faces is calculated using interpolation with halo nodes [25]. Figure 3.5 displays the control volumes on two sides of the interface. The blue control volume is the host/parent with *I* as the control volume center. The projected control volume center on the normal to the face center F_l is I'. A halo node E is generated when I' is reflected through the face center F_l. The value of any variable ϕ at that face F_l is calculated by:

$$\phi_{F_l} = \frac{\phi_{I'} + \phi_E}{2} \tag{3.12}$$

ϕ_E is found by identifying the center of the nearest control volume close to E. This center in Figure 3.5 is denoted A which is the halo control volume center. In the next step, the value at A is extrapolated to E:

$$\phi_{F_I} = \phi_A + \underline{AE}.(\nabla\phi)_A \tag{3.13}$$

In a similar way the value $\phi_{I'}$ is computed by extrapolating from the host control volume center *I*. For this technique to work properly, the halo node must be positioned in the control volumes close to the interface. Hence, when the mesh was generated, special care was taken to ensure that the control volumes on both sides of the interface were of the same depth. The time step for the simulations was chosen in a similar manner such that the halo nodes do no skip control volumes in the neighboring region.

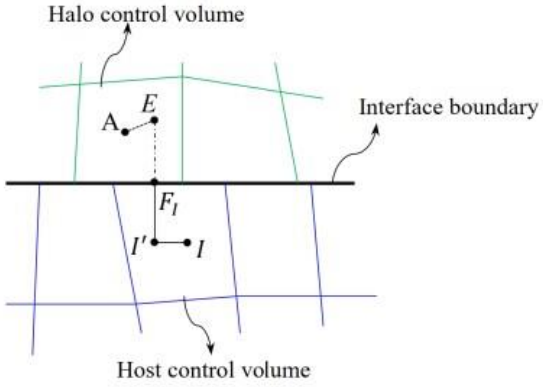

Figure 3.5: Halo and host control volumes across interface

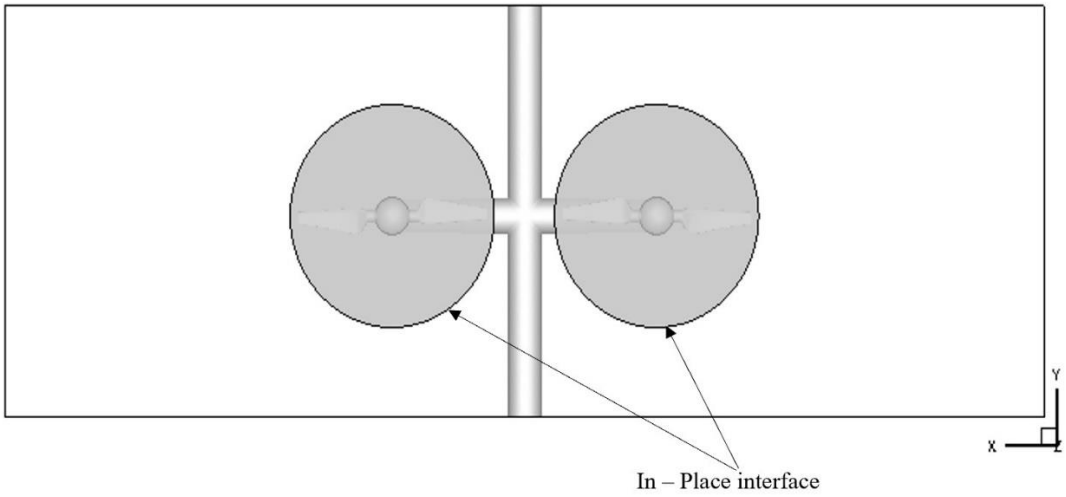

Figure 3.6: In-Place Interface

3.5 TURBINE GEOMETRY AND VALIDATION DATA

3.5.1 *Turbine geometry*

The comparisons made in this thesis are made against experiments conducted in an open channel facility at the University of Minnesota's St. Anthony Falls Laboratory (UMN-SAFL). The turbine used is the 1:40 geometric scale modified version of the Department of Energy's Reference Model-I (RM) of MHK technology. It is a dual rotor axial flow horizontal axis device with counter-rotating rotors, each with a diameter of D = 0.5m. Along with the rotor blades, other components of the turbine were also included in the simulations, namely, a central monopile, horizontal support structures, nacelles, and hubs. Figure 3.7 shows in the whole assembly along with the dimensions of each component. Detailed information of the model is given in

Table 3.3. The three-dimensional model of the geometry was created in SolidWorks and the surface mesh of each component was imported in StarCCM+ for the simulations. The blade profile used is the NACA-4415. The characteristics of this airfoil are mentioned in Table 3.2

.

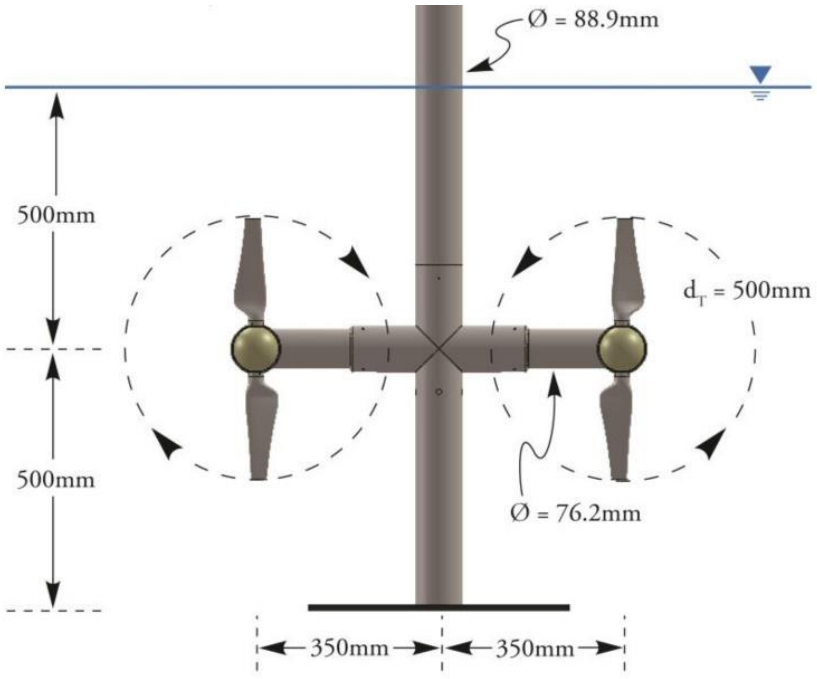

Figure 3.7: Turbine configuration

3.5.2 *Turbine Performance*

To verify the predictions for the coefficient of power (C_p, given by eq (3.17)) given by the CFD simulations, they are compared with the measurements made in the open channel experiment. Measurements of the turbine performance in the channel were collected at a speed of ~1.045 m/s, for a range of tip speed ratios, TSR or λ, given by eq (3.14), from approximately 2 to 8. The channel has a length of 85 m, a width of 2.75m and a height of 1.8m. For the simulations, the water height was maintained at 1m, equal to the experiments. These dimensions account for a blockage ratio of 14.3%. For more details on the experimental setup and analysis refer to Hill et al. [39].

$$\lambda = \frac{\omega R}{U_\infty} \tag{3.14}$$

Table 3.2: Characteristics of the 1:40 RM1 SAFL model turbine NACA 4415 blade

r/R	Radius	Pre-Twist	Chord	% Thick	Thickness
(-)	(mm)	(deg)	(mm)	(t/c)	(mm)
0.21	53.3	13.16	30.0	100.0	30.0
0.24	60.0	13.16	30.0	100.0	30.0
0.27	66.7	13.16	34.2	84.9	29.0
0.29	73.3	13.16	46.8	51.8	24.2
0.32	80.0	13.16	57.2	31.1	17.8
0.35	86.7	13.16	62.6	19.4	12.1
0.37	93.3	13.16	64.5	15.0	9.7
0.40	100.0	11.28	64.4	15.0	9.7
0.43	106.7	10.24	63.2	15.0	9.5

0.45	113.3	9.43	61.5	15.0	9.2
0.48	120.0	8.76	59.5	15.0	8.9
0.51	126.7	8.17	57.4	15.0	8.6
0.53	133.3	7.64	55.3	15.0	8.3
0.56	140.0	7.16	53.2	15.0	8.0
0.59	146.7	6.70	51.1	15.0	7.7
0.61	153.3	6.27	49.2	15.0	7.4
0.64	160.0	5.86	47.3	15.0	7.1
0.67	166.7	5.46	45.6	15.0	6.8
0.69	173.3	5.07	44.0	15.0	6.6
0.72	180.0	4.69	42.4	15.0	6.4
0.75	186.7	4.31	40.9	15.0	6.1
0.77	193.3	3.93	39.5	15.0	5.9
0.80	200.0	3.55	38.2	15.0	5.7
0.83	206.7	3.17	37.0	15.0	5.5
0.85	213.3	2.78	35.8	15.0	5.4
0.88	220.0	2.38	34.6	15.0	5.2
0.91	226.7	1.98	33.5	15.0	5.0
0.93	233.3	1.57	32.3	15.0	4.9
0.96	240.0	1.14	31.2	15.0	4.7
1.00	250.0	0.70	30.0	15.0	4.5

Table 3.3: Turbine model dimensions

Parameter	SAFL Turbine Geometries
Blade Profile	NACA 4415
Max Chord Length	0.0645 m
Tip Chord Length	0.0312 m
Rotor Diameter (D)	0.5 m
Hub Height (h_{hub})	0.5 m (1.0 D)
Hub Diameter (d_{hub})	0.087 m (0.174 D)
Hub Length (L_{hub})	0.080 m
Nacelle Length (L_N)	0.380 m
Nacelle Diameter (d_N)	0.095 m (0.19 D)
Cross Arm Diameter	0.0762 m
Vertical Tower diameter	0.0889 m
Rotor Spacing (S)	0.7 m (1.4 D)

For this project, the turbine performance was characterized using the following parameters:

- Turbine power (P_T). Turbine power is defined as the product of the rotor torque and angular velocity, as given by eq (3.15.)

$$P_T = \tau\omega \tag{3.15}$$

Where τ is the torque for each rotor measured at each time step and averaged over one revolution of the rotor and ω is the blade angular velocity.

- Available Power (P_A) of the incoming flow was calculated using the freestream velocity:

$$P_A = \frac{1}{2}\rho A_T U_\infty{}^3 \tag{3.16}$$

Where ρ is the density of water ($\approx 1000\, kg/m^3$), A_T is the rotor swept area and U_∞ is the freestream velocity.

- Coefficient of performance (C_p) is calculated as the ratio of the power values described above, using:

$$C_p = \frac{P_T}{P_A} \tag{3.17}$$

3.5.3 *Wake Profiles*

The wake measurements were compared with the experimental values measured by acoustic doppler velocimetry at various distances downstream of the turbine (1 to 9 diameters from the turbine axis). The wake velocity recovery downstream of the turbine was reported using the streamwise velocity deficit ($\overline{U}_{def}$), defined as follows:

$$\overline{U}_{def} = \frac{\overline{U}_\infty - \overline{U}_x}{\overline{U}_\infty} \tag{3.18}$$

Where $\overline{U}_\infty$ is the freestream velocity at hub height, or rotor height center and $\overline{U}_x$ is the hub height velocity at a position z downstream of the turbine.

The momentum deficit calculated along the streamwise direction is another metric used to define the wake profile, which is calculated from the velocity deficit as follows:

$$M_{def} = \int_z \frac{\rho\overline{U}_\infty - \overline{U}_x}{\rho\overline{U}_\infty} \cdot \frac{\overline{U}_x}{\overline{U}_\infty} dz \tag{3.19}$$

3.6 DOMAIN GEOMETRY

The background region or the channel domain was created to match the dimensions of the flume in width as well as the water height from the experiments. The computational domain was designed with an inlet close to the vertical support structure, and an outlet far downstream for detailed wake analysis. Figure 3.8 shows the channel domain with the distance from the inlet to the axis of the vertical support as 3D and from the outlet to the rotor disk, for the wake, as 10D, where D is the diameter of the turbine rotor. The bottom and sidewalls of the domain along with the turbine support structure were modeled as no-slip boundaries, since the experimental boundary layers on the channel walls could not be simulated, and played no role in the experimental results as they are thin for this high Reynolds number channel flow.

The Froude number for the simulations, calculated using eq (1.5), matches the experimental value of 0.33. The characteristic length scale used for calculating F_r is the depth of water, which is the length scale commonly used for open channel flows. This value is low enough to justify that the

deformations of the free surface due to the presence of the turbines is small and therefore can be neglected in the simulations [40]. As modeled by Adamski and Aliseda [40] and Turncock [19], the free surface is represented as a symmetry plane wall boundary with zero shear. This assumption is justified as follows:

$$\frac{\mu_{air}}{\mu_{water}} \frac{\partial V_{air}}{\partial z}\Big|_{z=\text{interface}} = \frac{\partial V_{water}}{\partial z}\Big|_{z=\text{interface}} \approx 0 \tag{3.20}$$

Where μ is the fluid viscosity, V is the fluid velocity, and z is the vertical direction. At the free surface interface, the shear in the air equals in the shear in the water. Since the viscosity of water is much greater than that of air, shear is approximately equal to zero at the interface on the waterside, and the boundary can be assumed as a free shear boundary that neglects any surface fluctuations as shown by eq (3.20) [4].

A velocity inlet and a pressure outlet were used for the channel. The turbulent length scale l is a physical quantity related to the larger eddies present in the flow[8] The value of l for channel flows is commonly defined as

$$l = 0.07 D_h \tag{3.21}$$

Where D_h is the hydraulic diameter is given by

$$D_h = \frac{2w * h}{w + h} \tag{3.22}$$

Where w is the channel width and h the channel height. The l value used in these simulations is 0.2D, where D is the turbine diameter. The inlet was initialized using values of turbulent kinetic energy, k, of 0.0034 m^2/s^2 observed in the experiments, and turbulent dissipation rate, ε, 3E-4 m^2/s^3 evaluated using the turbulent length scale l and k, given by eq (3.23)

$$\varepsilon = C_\mu^{3/4} \frac{k^{3/2}}{l} \tag{3.23}$$

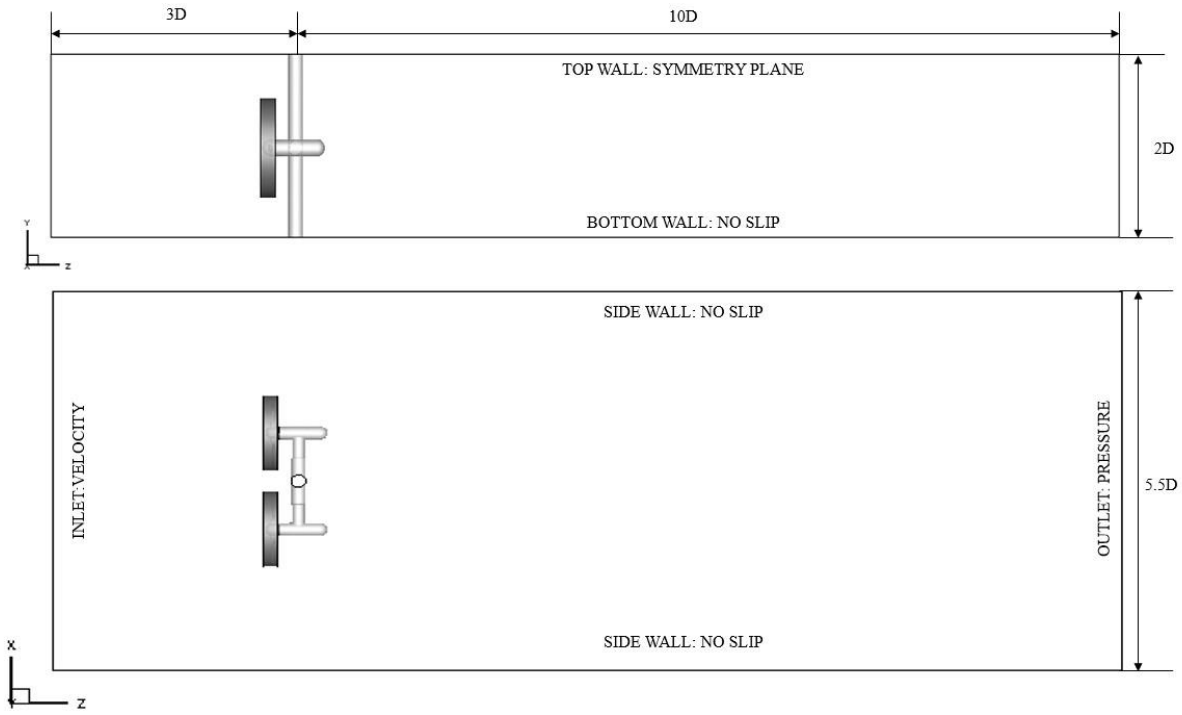

Figure 3.8: Channel domain top and view

Where C_μ is a turbulence modeling constant based on Kolmogorov scaling. The inlet velocity was set to match the experiments at 1.045 m/s. The outlet was initialized with the same turbulent length scale and *k* value as the inlet and constant pressure of 0 Pa (gravity is neglected and hydrostatic pressure does not play a role). Two identical cylindrical domains were created for the rotating regions around each turbine rotor, to implement the sliding mesh model as mentioned in the previous section, extending to a radius of 0.27 m from the rotor axis, where R=0.25 m is the radius of the rotor, and a thickness of 0.087m, beginning from the intersection between the rotor and the hub. Figure 3.9 shows the two rotating subdomains extracted from the background regions. The walls of the cylinders were set as in-place interfaces with the rotors modeled as no-slip boundaries.

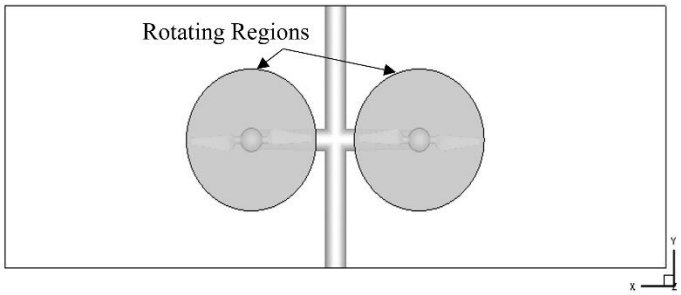

Figure 3.9: Rotating subdomains surrounding the turbine blade

The region surrounding the right rotor is prescribed with clockwise motion, and the one surrounding the left rotor is specified with anticlockwise movement to model the counter-rotating effect. The modeled blockage ratio was kept consistent with the experiment at 14.3%.

3.7 MESH GENERATION

In CFD, the process of mesh generation plays a crucial role in determining the accuracy of the solution. The accuracy of the mesh increases with increasing number of cells. However, as the mesh becomes finer, this also increases the computation time. The key to an effective and accurate solution is to obtain a balance between the need for higher spatial discretization and the cost of a longer solution time. By selecting a very fine mesh, it is possible to achieve a negligible gain in the simulation accuracy, but if the mesh is under-resolved, we would surely get incorrect results. Since StarCCM+ is a finite volume solver, the computational domain is spatially discretized into small elements to solve the discrete difference equations. An unstructured tetrahedral volume mesh is generated for both regions that divide the domain into tetrahedral volumes. We use an unstructured grid as it takes less time to generate the mesh while giving satisfactory results. Prismatic layers were created at the no-slip boundaries of the domain to resolve the wall for analysis of the boundary layer.

The global element size for both regions was set to 0.5 m with a surface curvature of 200 pts/circle. The target size of 5% of the global element size was set for the rotating regions with a minimum size fixed at 1% of the global size. Cells within the rotating region were set to grow at an overall rate of 2.0. Since we are using near-wall modeling to capture the boundary layer at the blade, a very fine mesh is required near the rotor surface. In order to meet the requirement of $y^+ \sim 1$, the first node distance to the wall was 0.007 mm for the mesh surrounding the two rotors. A grid

independence study was conducted before selecting this value, which is discussed in more detail in the next chapter. The prismatic layer was designed with a total of 6 cells in width, with an overall thickness of 0.001m, and each prismatic layer stretching 2.0 times the original cell size to meet the requirement for the boundary layer as seen in Figure 3.10.

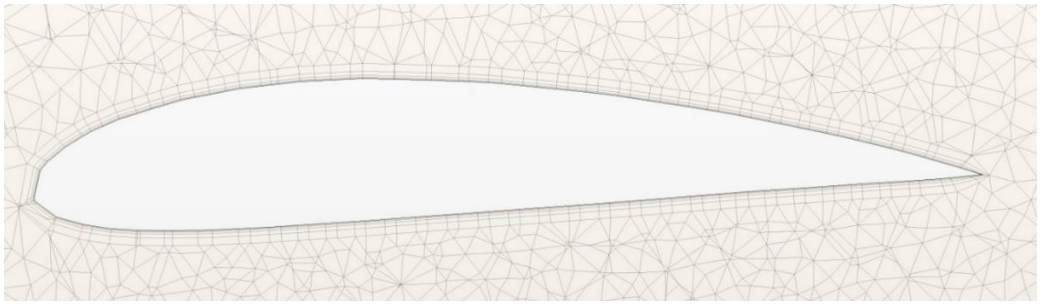

Figure 3.10 Mesh near surrounding the blade using the near-wall modeling approach

The elements in the background region were set with a target size of 10% and a minimum size of 5% of the cell base size. The subsequent cells were fixed to grow at a rate of 2.5. The prismatic layer for this region was designed with three cells width, an overall thickness of 3% and an overall stretching of 2.0. In this thesis, we are mainly interested in the boundary layer developed at the turbine blades, hence in order to reduce computation time, no prismatic layers were created for the turbine support structure. As the results did not depend on the velocity gradient in the boundary layer formed at the bottom and side walls being realistic, a comparatively coarser mesh was used to reduce memory and CPU requirements. For a better understanding of the wake dynamics, the volume surrounding and behind the turbine was refined with various volume controls as shown in Figure 3.11 with a finer mesh in the near and far wake regions.

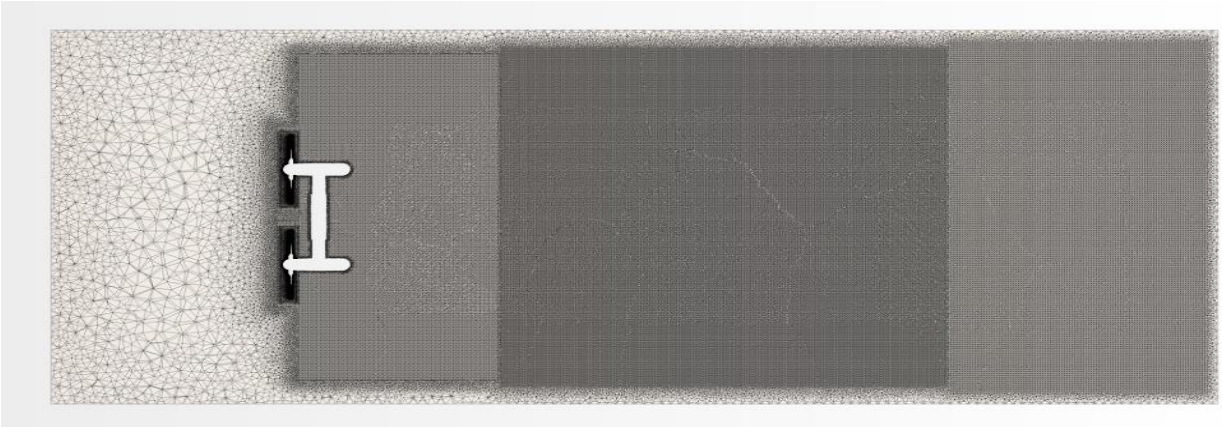

Figure 3.11: Mesh in the xz plane across the turbine

Additionally, the cells at the interface boundaries were fixed at minimum and target size of 0.005m to limit the numerical error across the surface. As suggested by McNaughton et al. 2014 [25], in this sliding mesh computations, the time step for each simulation was chosen so that the maximum sliding distance (at the outer radius of the rotating region) would not be more than the half a control volume of one cell. A 1.15-degree rotation per time-step was found to be adequate to capture the flux across the rotating and stationary regions to simulate flow across the turbine as it ensured for each time step the sliding distance is not more than one cell width.

3.8 NUMERICAL MODEL SETTINGS

The most critical settings and solution techniques for validation of the results with experimental data are presented in Table 3.4. For stable and converged solutions with the sliding mesh model, the rotational speed of the turbine was gradually increased. This ensured that large complex forces were not induced in the flow with a sudden increase in angular velocity. The freestream velocity was also raised in parallel to the rotating speed of the turbines, to avoid flow separation along the blade due to large angles of attack, that would produce non-physical results [3].

Table 3.4: Sliding mesh model settings and solution methods

Solver type	Implicit Unsteady
Turbulent Models	Realizable $k-\varepsilon$ Two-layer method
Pressure-Velocity Coupling	SIMPLE
Discretization of Gradient	Hybrid Gauss- Least Square Method
Discretization of Time	Second-order Upwind
Discretization of Pressure	Second Order
Discretization of Momentum	Second-Order Upwind
Discretization of Turbulent Viscosity	Second-Order Upwind
Discretization of Turbulent Kinetic Energy	Second-Order Upwind
Discretization of Turbulent Dissipation Rate	Second-Order Upwind
Pressure Under-Relaxation Factor	0.2
Velocity Under-Relaxation Factor	0.8
Turbulent Viscosity Under-Relaxation Factor	0.1

Chapter 4. RESULTS AND DISCUSSION

4.1 MESH INDEPENDENCE STUDY

The mesh independence study was performed for the rotating regions at a λ of 5.07. The three grids considered are described in Table 4.1. The hydrodynamic torque averaged over one revolution, for both rotors is computed in each mesh. As the blades rotate, the shear experienced by the flow inside the blade boundary layer is resolved in the rotating reference frame, and does not correspond to the shear in an inertial frame of reference, which is the basis for the wall modeling functions used in boundary layer RANS simulations. Due to this effect, the empirical relations used in the wall function approach face difficulty in modeling the boundary layer near the blade [4]. Hence the viscous layer must be resolved by the grid in order to accurately simulate the flow around the blades. Therefore, near wall modeling technique is used, as the best suitable to capture the physics within the boundary layer near the blades. All mesh configurations are designed using the near wall modeling approach for the boundary layer, as described Chapter 3.

Table 4.1: Mesh grids for the rotating regions

Mesh Number	Type		First Node from wall (in mm)
1	Coarse	Right Rotor	0.0158
		Left Rotor	0.0158
2	Medium	Right Rotor	0.007
		Left Rotor	0.007
3	Fine	Right Rotor	0.003
		Left Rotor	0.003

To validate the mesh, the streamwise velocity contours from 1D upstream of the turbine to 5D downstream of the turbine are plotted across horizontal plane at y = 0 at λ = 5.07. From the three cases considered, the results recorded from the medium and fine mesh show minimal difference in the velocity gradients as seen in Figure 4.1. The high velocity pockets near the rotors representing the tip and root vortices are captured better in the medium and fine meshes compared to the coarse mesh. We decided that mesh 2 with medium refinement was the optimum trade-off between computation time & cost and simulation accuracy and therefore used it for conducting all

subsequent simulations in this thesis. The medium resolution not only provided sufficient refinement to capture the flow behavior in the viscous layer near the blade surface but also kept computation memory and simulation run times within tolerable limits.

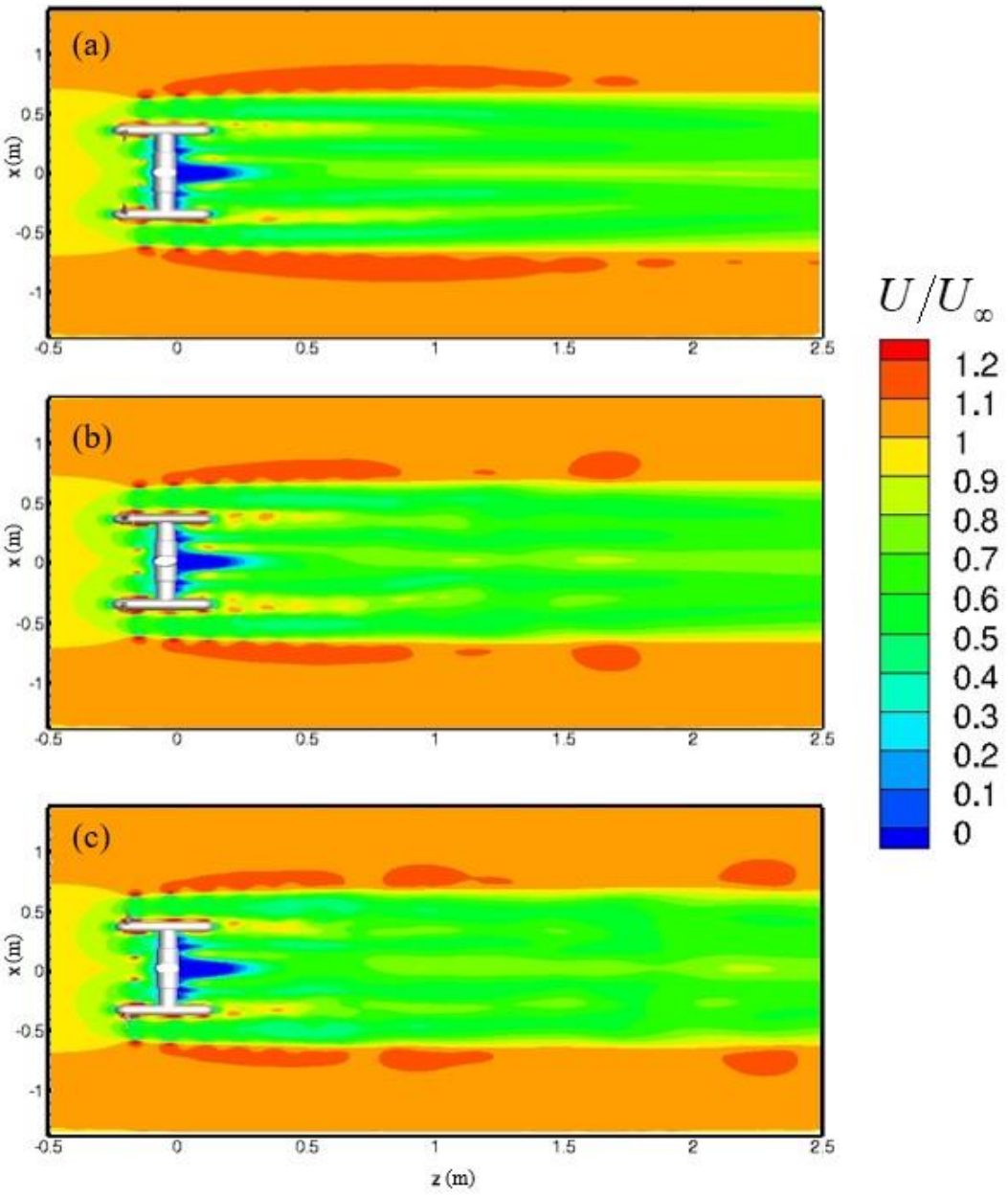

Figure 4.1: Streamwise velocity contours at $\lambda = 5.07$ in y = 0 plane: (a) Coarse mesh, (b)Medium mesh and (c) Fine mesh

4.2 MODEL VALIDATION

4.2.1 *Turbine Performance*

Figure 4.2 shows a plot of the power curves for left and right rotor from the experiments and the data from the simulations. Simulations are conducted for tip speed ratios varying from 2 to 9 at a constant inlet velocity of $1.045\,m/s$. Instantaneous torque is measured at each blade surface element and averaged over the surface of each rotor. Once the simulation stabilizes after every increment in angular velocity, the torque is averaged over one complete revolution and multiplied by the rotor angular speed to calculate the mean turbine power ($\overline{P_T}$) used in C_p calculations. We can observe very good qualitative agreement between the experiments and simulations. Both rotors peak at λ = 5.07, as in the experiments. For larger TSR values, there is a drop in the rotor's performance. As the TSR increases for a given freestream velocity, the angle of attack decreases and the lift and drag forces act almost perpendicular and parallel to the blade respectively. More of the flow is diverted away from the blade, due to the higher effective solidity ration of the faster spinning blades, thereby reducing the rotor efficiency [21].

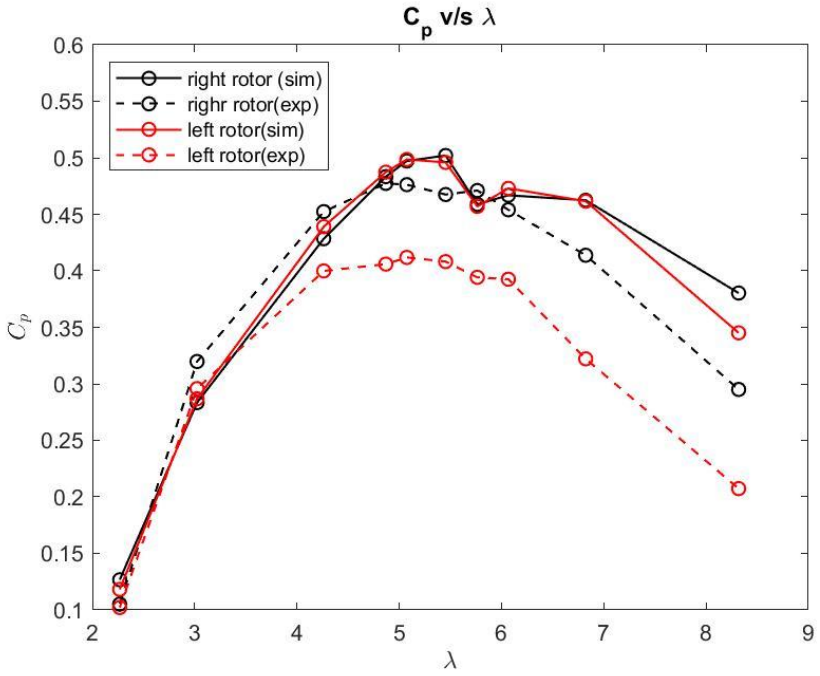

Figure 4.2: Calculated turbine power curves for both rotors: experiments (dotted line) and simulation (solid line)

We observe that although both rotors perform at a relatively high level, a substantial discrepancy is recorded in the experiments for the left rotor as compared to the right rotor. Hill et. all [39] hypothesized that the complexity of the flow in the channel and a slight asymmetry of the incoming flow may have caused this difference in values. In addition, uncertainties encountered while taking the measurements also may have been a factor causing this variation. As C_p is a function of U^3, even small differences in free stream velocity, a difference of 0.03 – 0.05 m/s (that is $\approx$ 3 - 5% for the RM1 experiments) , would result in 9-15% difference in performance values as seen in Figure 4.2: Calculated turbine power curves for both rotors: experiments (dotted line) and simulation (solid line). Along with the overall asymmetry in the incoming flow, even a difference in velocity of flow approaching on both sides of the ADVs used to measure instantaneous C_p may have played a role in propagating this discrepancy. Therefore, the performance curves from the right and left rotors in the experiments show a difference of 10%. However, such behavior is not observed in the simulation results. In simulations, the flow is modeled as a uniform inlet without any asymmetry and complexity. The measurement uncertainty is also negligible in simulations, compared to experiments. Both rotors perform with almost identical values, as expected.

4.2.2 *Wake characteristics*

The streamwise velocity deficit at rotor hub height (plane y = 0) was calculated at various distances downstream of the turbine ranging from 1D to 9D in intervals of 1D from the turbine blades. Mean velocity measurements were recorded for the optimal TSR value of 5.07. Data recoded was compared with the experimental results as shown in Figure 4.3,Figure 4.4 and Figure 4.5. In general, the velocity profiles from the CFD analysis show good agreement with the experimental results. The largest velocity deficit occurs for both the cases in the wake of the central monopile at 1D and 2D downstream from the turbine center for the experiments and simulations respectively. The largest velocity deficit for experiments occurs in the wake around the center of the central support tower, around 80%, as seen in Figure 4.3 (a) due to strong von Karman vortices shed from the cylindrical monopile, though the simulations underpredict this maximum value by around 30%. As we go further downstream, around 2D to 3D, we observe three peaks in the plot. These are produced in the low momentum regions of the central monopile (x= 0) and the center of the rotors

(x =0.35, x =-0.35). These are the regions that experience mixing of high momentum fluid that goes through the center of the rotors and around the monopile with low momentum fluid from the flow through the blade and monopile wakes. This phenomenon occurs around 2D downstream for experiments but is predicted further downstream, at 3D, for the simulations, as seen in Figure 4.4.

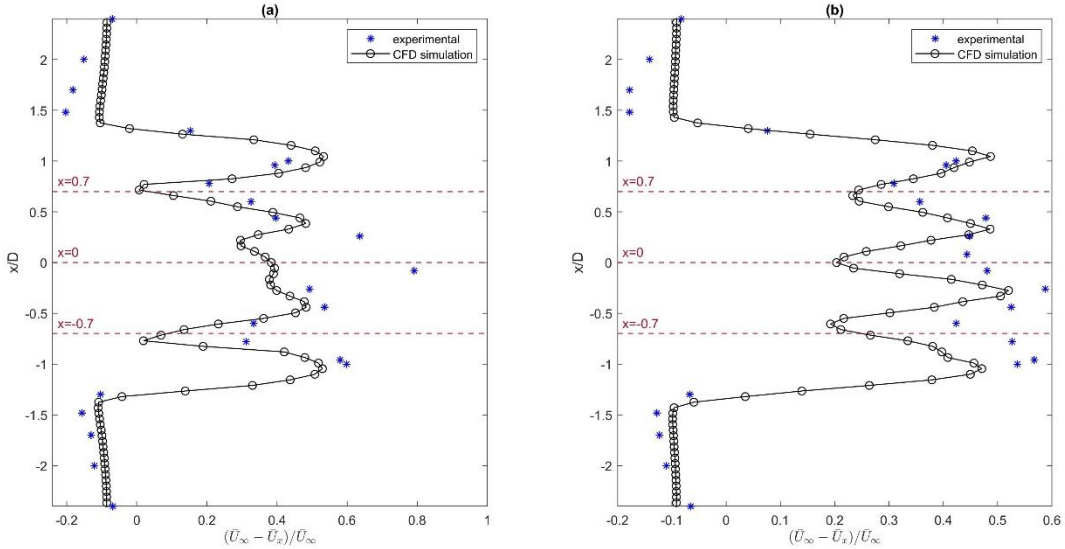

Figure 4.3: Velocity deficit - (a) 1D downstream, (b) 2D downstream of the turbine

The flow instabilities generated by the support structure increase the rate of mixing and lead to an increase in wake mixing and a decrease in the recovery distance. These instabilities are not captured by the turbulence closure model used in these RANS simulations, where the central monopile is under resolved, as it is not the focus of this study. Due to this delay, we see that the two minima at the center of the rotors still persist in the simulations up to 4D and disappear at 5D while for the experiments they disappear at 3D. We see the centerline minima vanish in the experiments at 5D, and the velocity wake presents a Gaussian shape. However, for the simulations, this minimum persists till 9D, as seen in Figure 4.5. The reason for this inconsistency between experiments and simulations could be propagated due to the low-resolution mesh used to predict the flow around the central monopile and the turbine support structure. A coarsely refined mesh was used around these regions as a tradeoff between solution accuracy and computation resources. One of the main drawbacks of the $k-\varepsilon$ model is that it is unable to capture the flow instabilities near the wall if the region is not well resolved. Hence, the turbulence properties of flow around the support assemble are not accurately predicted in the simulations, and limited mixing in this area causes the centerline minima to still exist up 9D downstream of the turbine.

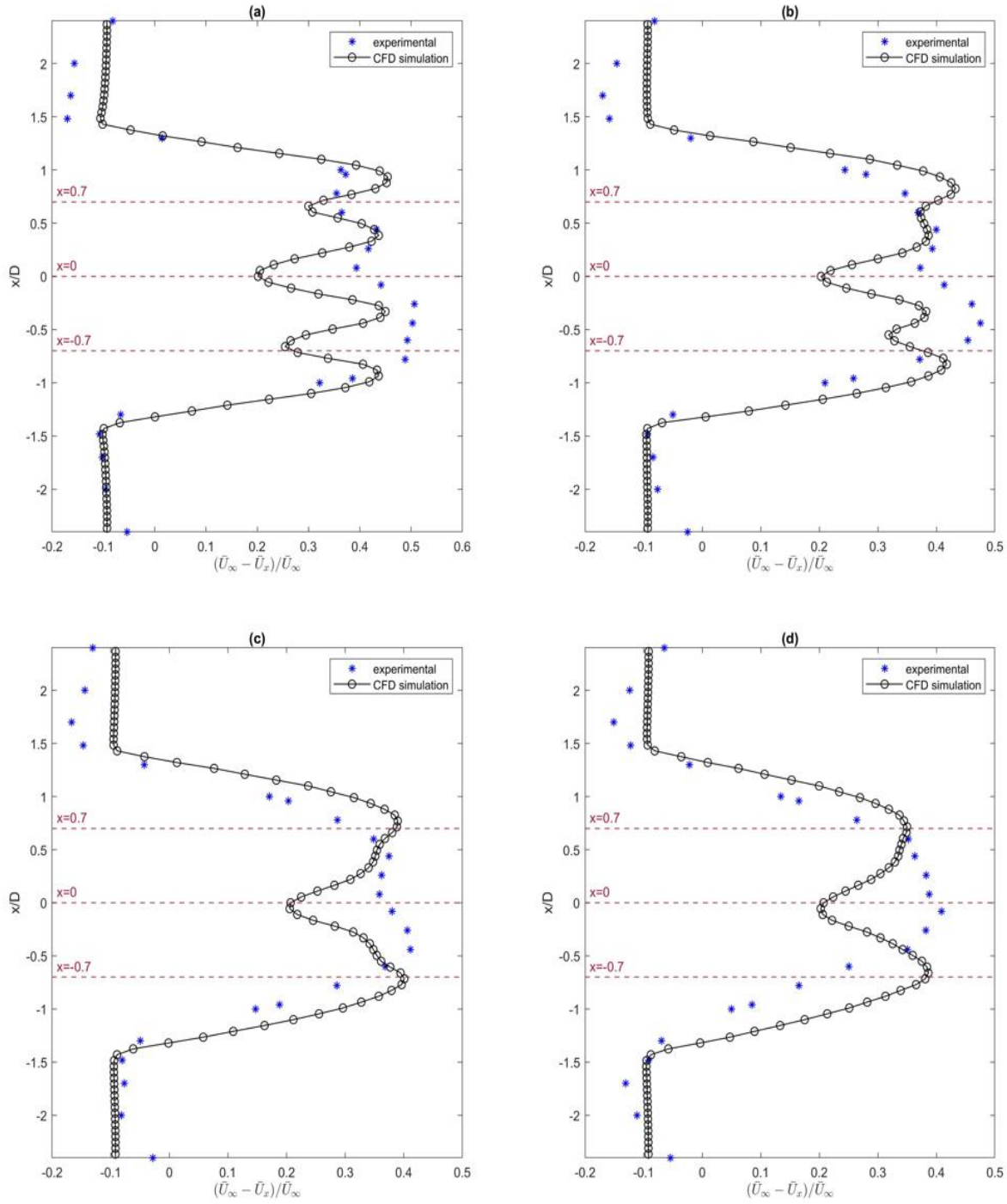

Figure 4.4: Streamwise velocity deficit at hub height: (a) 3D (b) 4D (c) 5D and (d) 6D downstream from turbine center

The delayed mixing also influences the overall width of the wake. We see that the wake looks wider for the simulations as compared to the experiments starting around 4 to 5D as the high

velocity region in the center of each turbine must compensate the low velocity region near the monopile which leads to a difference in velocity recovery. At 9D, the maximum velocity has recovered to about around 66% in the simulations compared to 70% in the simulations. Due to the large blockage by two horizontal supports and the central vertical tower, a wide wake propagates as we go further downstream.

Asymmetry in the incoming flow, as discussed in the previous section, is also seen in the velocity deficit recorded in the experiments. We see that the plots from 1D to 9D are asymmetric for experiments while the simulations do not display this feature. From 1D to 5D, asymmetry exists in the velocity deficit around the turbine structure, but it disappears at 6D. However, the asymmetry in the velocity of flow between the channel walls and the turbine structure is still seen up to 9D for the experiments. We see that the effects of asymmetry no longer influence the wake recovery, as the dominant phenomenon in this region is enhanced turbulent mixing, which depends mainly on the turbulent intensity and flow perturbations upstream of the turbine.

Figure 4.6 illustrates the streamwise momentum deficit plotted at hub height (X=0 plane) for both experiments and simulations. The values for both cases were calculated at peak turbine power i.e. TSR of 5.07. The momentum deficit was calculated for a range of 1D to 9D downstream of the turbine. The integral of the momentum flux was derived using the trapezoidal rule. The values obtained through the simulations show reasonable agreement with the experimental data. In general, we observe that the highest deficit of momentum occurs just behind the turbine at around 1D to 2D and then slowly recovers as we go downstream. This loss of momentum in the flow is the direct result of the drag force acting on the two turbine rotors, the central tower and support structures. The integrated momentum deficit is the measure of the total drag force induced on the turbines. We observe that maximum momentum deficit in the experiments occurs at 1D downstream of the turbine in the region behind the central monopole, reaching a value of 47%. This value recovers as we go downstream and high momentum fluid from the outer bypass flow (faster than the free stream velocity) mixes with the wake, reaching 15% of the incoming momentum flux at 9D. This corresponds to the velocity deficit results discussed in the previous section This is due to the low velocity, high mixing region behind the vertical support structure.

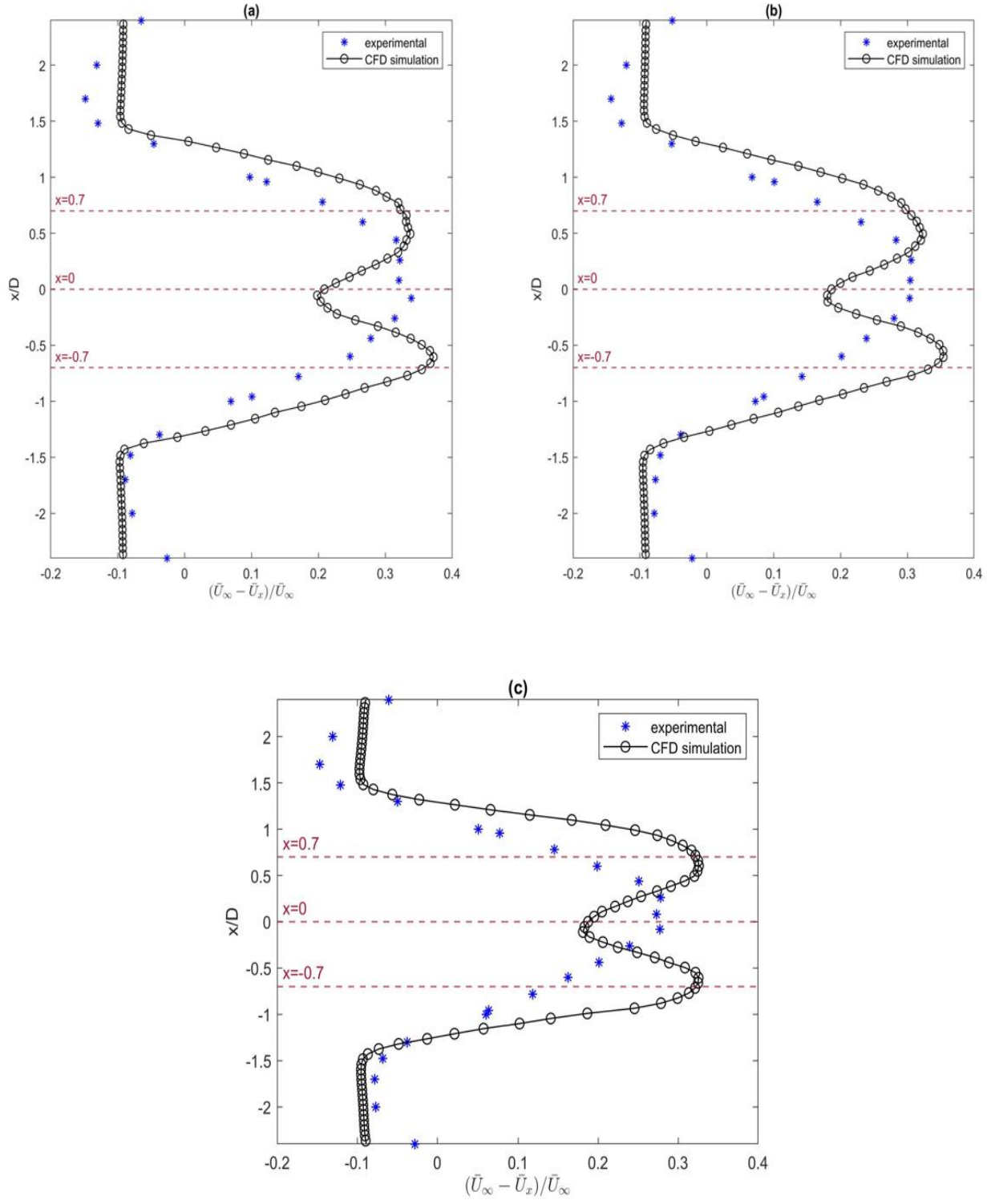

Figure 4.5: Streamwise Velocity Deficit: (a) 7D (b) 8D and (c) 9D downstream of the turbine center

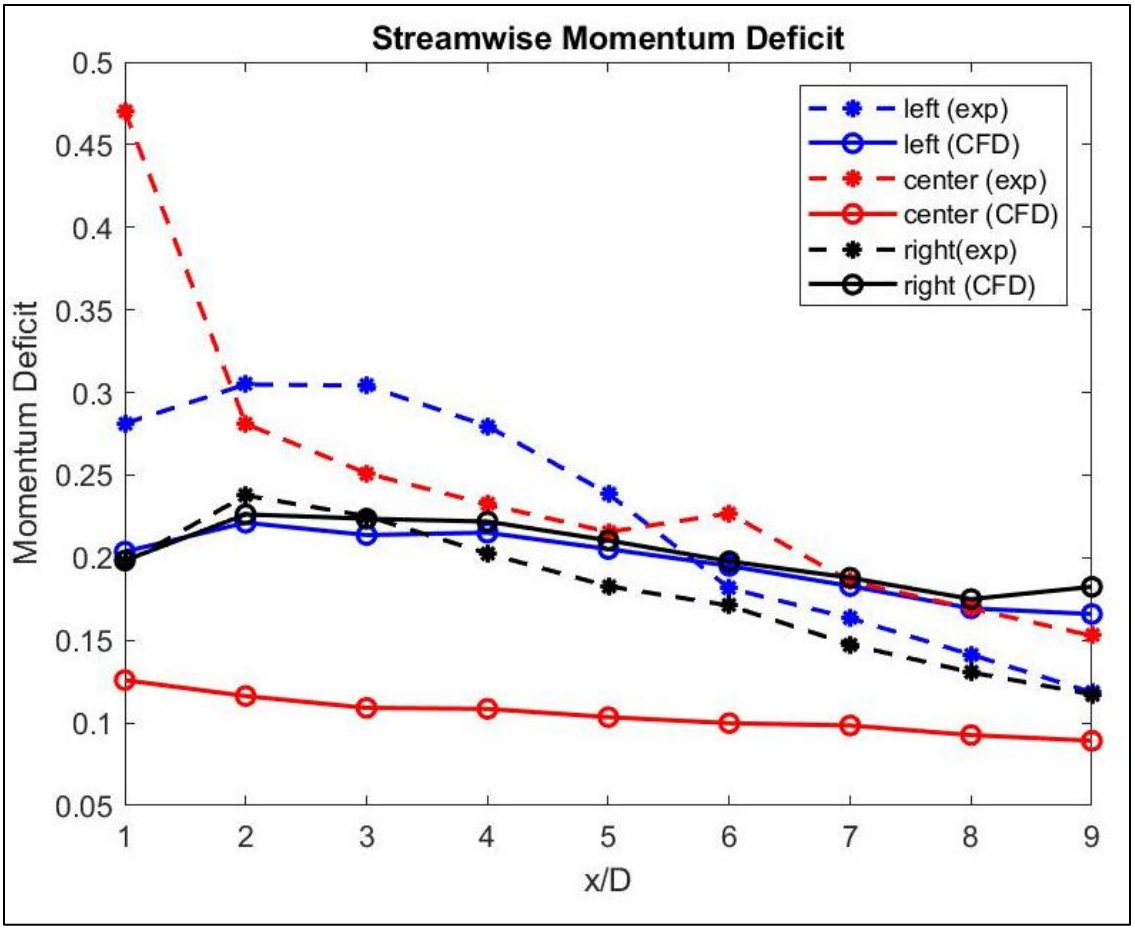

Figure 4.6: Streamwise momentum deficit for experiments (dotted) and simulations (solid)

The high blockage provided by the support structure also contributes to this difference in momentum. However, this effect is not recorded by the simulations as seen in Figure 4.6. We see that, compared to the experiments, the momentum deficit for the region surrounding the monopile is only 13%. As we go further downstream, we see that mixing is not intense, and there is not much change in the values with the wake recovering only to within 8% of the original momentum. The rate of recovery for the simulations in this region is not as drastic as that observed in simulations Due to low mesh resolution in this region, mixing is underpredicted, which could be the reason for this variation. The peak momentum deficit for the rotors in both experimental as well as simulation cases occurs at 2D downstream, and this is gradually recovered as the we go downstream from the turbine. At 9D the momentum recovers to about 11% for the experiments and around 16 - 18 % for the simulations. The recovery is much faster for the experiments. As discussed in the previous section, the larger momentum deficit is due to the reduced mixing for simulations, resulting in wider wakes and longer recovery distances. The effects of asymmetry in upstream flow in the open

channel can be observed as a larger momentum deficit for the left rotor. This variation can be observed up to 5D downstream after which the wake becomes symmetric. From 6D to 9D the effect of mean flow on the velocity recovery is minimal. The main mechanism affecting the wake recovery is the vortex system breakdown due to turbulent mixing.

4.2.3 *Lateral expansion*

A section across the wake of the RM1 at mid-depth (y=0) shows the lateral velocity profile of the wake for simulations and experiments. Contour plots of the mean streamwise velocity at rotor hub height are shown in Figure 4.7 and Figure 4.8, where values have been normalized by the corresponding upstream flow velocity. Figure 4.9 shows the normalized velocity contours in three vertical planes, passing through the monopile and the center of the two rotors respectively, collected downstream of the turbine. As illustrated in Figure 4.7, the expansion of wake is symmetric with respect to the central axis for both simulations (a) and experiments (b). We observe a complex axisymmetric wake structure consisting of two regions for each rotor. We also see layers of high velocity surrounding the root and tips of each blade that represent the footprints of the root and tip vortices in up to 2D downstream. The inner wake region is formed due to the root vortices and the outer region is formed due to the tip vortices shed by the blades. In the Figure 4.8. The inner wake region can be described with the high velocity region at the center surrounded by an annular shaped high velocity deficit region. This high velocity is induced by the strong root vortices in the near wake region which moves towards the vortex core. The outer region which comprises of the tip vortices induce the flow outside the wake to accelerate forming a region of high velocity as the flow passes through the assembly. The largest velocity deficit occurs in the near wake regions at the center between the two rotors, immediately after the cylindrical horizontal support arms. This region is however more spread out for the experiments and exists up to 2D downstream of the turbine while it is found up to a relatively smaller distance of approx. 0.7D for the simulations as seen in Figure 4.7 and Figure 4.8 respectively. Due to the high blockage, the flow is accelerated outside each rotor as well as above and below the rotor. The wake of each rotor quickly joins the with the disturbance created by the central tower and forms an expansive wake that propagates downstream. Because of the presence of the channel walls, the wake expansion is confined and, after an initial widening, it remains approximately of the same width while slowly mixing with the surrounding flow. As we go downstream, the magnitude of velocity in the inner

wake decreases, mainly from 1D to 3D and remains almost constant thereafter. In the velocity contours across the vertical planes reported in Figure 4.9 (b) we see that the wake is symmetric about the turbine axis. The large velocity deficit concentrated around the area immediately behind the monopile structure is recovered at 2D from the turbine. We also observe the surrounding accelerated fluid in the bypass region created due to the adverse pressure gradient in the center of the channel as the flow passes through the turbine assembly, starts mixing with the low velocity region in the wake resulting in expansion of the wake above and below the turbine. In the flow surrounding the turbine rotors, we find low velocity regions in the contour behind the blades as a result of the energy extracted from the flow.

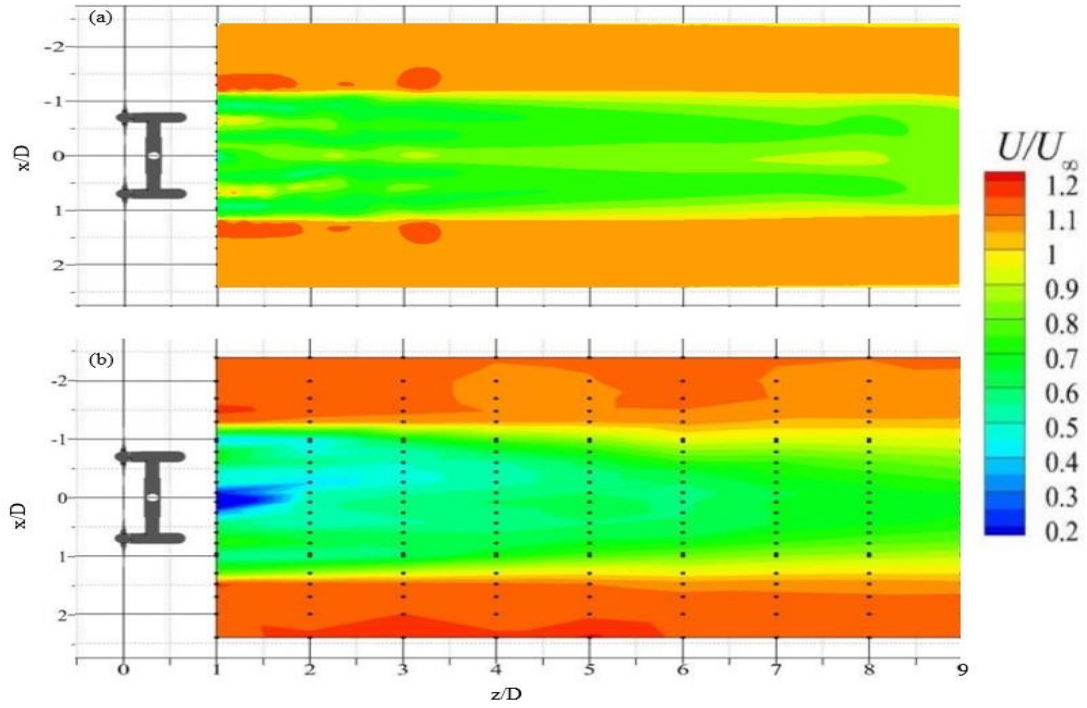

Figure 4.7: Normalized Streamwise velocity contours downstream of the RM1 at $\lambda = 5.07$ from 1D to 9D: (a) simulations and (b) experiments [33](Flow is left to right). The vertical dotted lines in (b) show actual ADV measurement profile positions

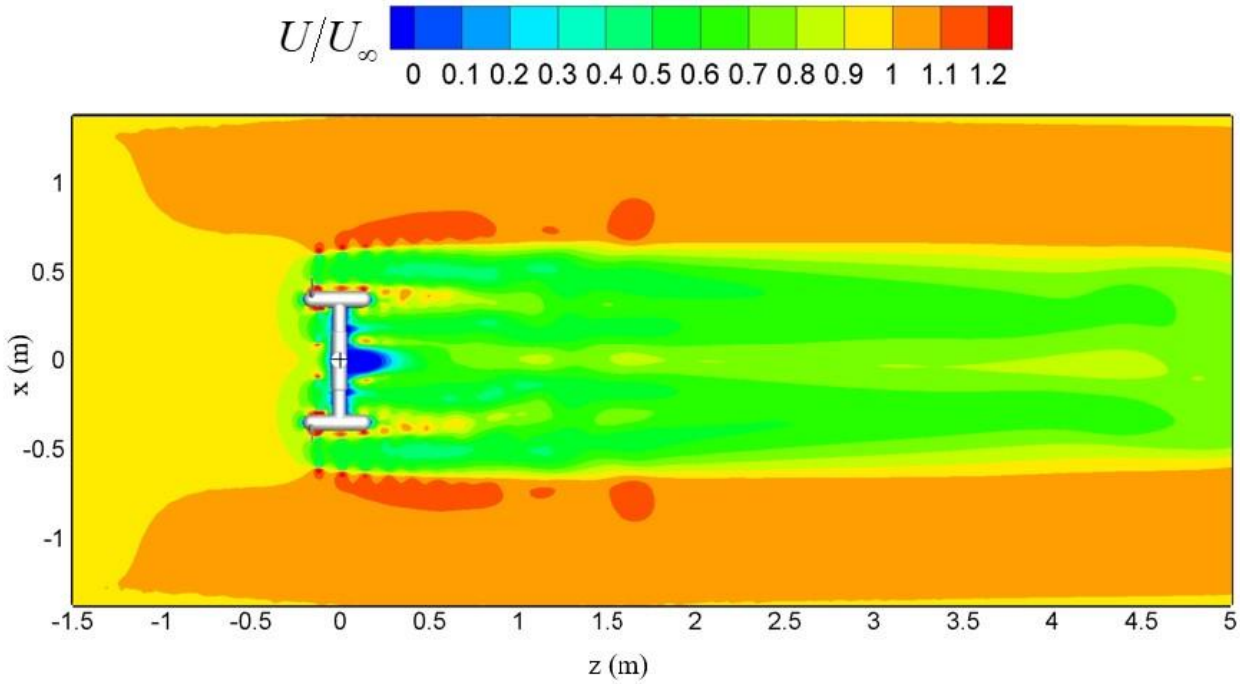

Figure 4.8: Normalized streamwise velocity (U_z) contour across the domain at mid plane (y = 0) for $\lambda = 5.07$ (simulations)

Normalized values of turbulent kinetic energy in the horizontal plane are reported in Figure 4.10 and Figure 4.11 Values of the normalized kinetic energy in the three vertical planes (through the center of the vertical tower and through each of the rotor's center) are shown in Figure 4.12. Elevated levels of TKE are seen in the downstream region, particularly extending up to 2D for the experiments and around 1.5D for simulations, which represents the high mixing region directly behind the turbine assembly. Due to the strong von Karman vortices shed by the cylindrical tower and horizontal arms, the levels of TKE are very high in the center of the wake, which instigates mixing in the experiments, closer to the turbine plane. Turbulence induced by turbine rotation is observed immediately behind the rotors, and it propagates downstream with the flow. The eddies shedding from the blades create regions of elevated TKE, as seen in Figure 4.11. High TKE is found in areas surrounding the top and bottom blade tips and roots for each rotor. We observe that from 2D to 4D, the TKE values start spreading in the vertical and horizontal directions. As seen in Figure 4.12. these pockets also indicate presence of a shear layer surrounding the low velocity region in the inner wake. As we go downstream, within the inner wake, the high TKE region representing the root vortices disappears at 3D for the simulations and 4D for the experiments as

depicted in Figure 4.10. This corresponds to the disappearance of the root vortices and onset of inner wake expansion [35]. Due to this merging the high TKE region surround the lower tip height starts to increase in the streamwise direction. Another effect of this merger is enhancement of turbulence mixing downstream of the turbine which is represented as the expansion of wake in the horizontal as well as the vertical planes. The wake in the vertical direction tends to move towards the free surface in the experiments but not in the simulations as seen in Figure 4.12(b) due to momentum transfer and mixing between the high velocity outside the wake and low velocity flow regions in the wake making it slightly asymmetric top to bottom. This meandering is not observed in simulations as for this project the effect of the free surface is not fully captured by the boundary conditions imposed. Overall the level turbulent kinetic energy recorded by the CFD simulations is lower than in the experiments. This discrepancy may be due to the turbulence closure model's inability to accurately compute generation of TKE at the blade and support structure walls. One of the limitations of the $k-\varepsilon$ model is its tendency to overpredict the decay in turbulence kinetic energy, which in this work causes the high TKE regions behind the turbine rotors to disappear in a short distance downstream in the simulations, while they still persist to at comparatively high values in the experiments[36]. In this project, the sliding mesh model is used to represent the effects of turbine rotation on the flow. It is possible that the TKE production on the rotor blades in under computed in the flow, due to idealized conditions on the rotating frame where separated flow does not occur on the root of the blades, which would contribute to these lower TKE levels in the simulations versus the experimental values.

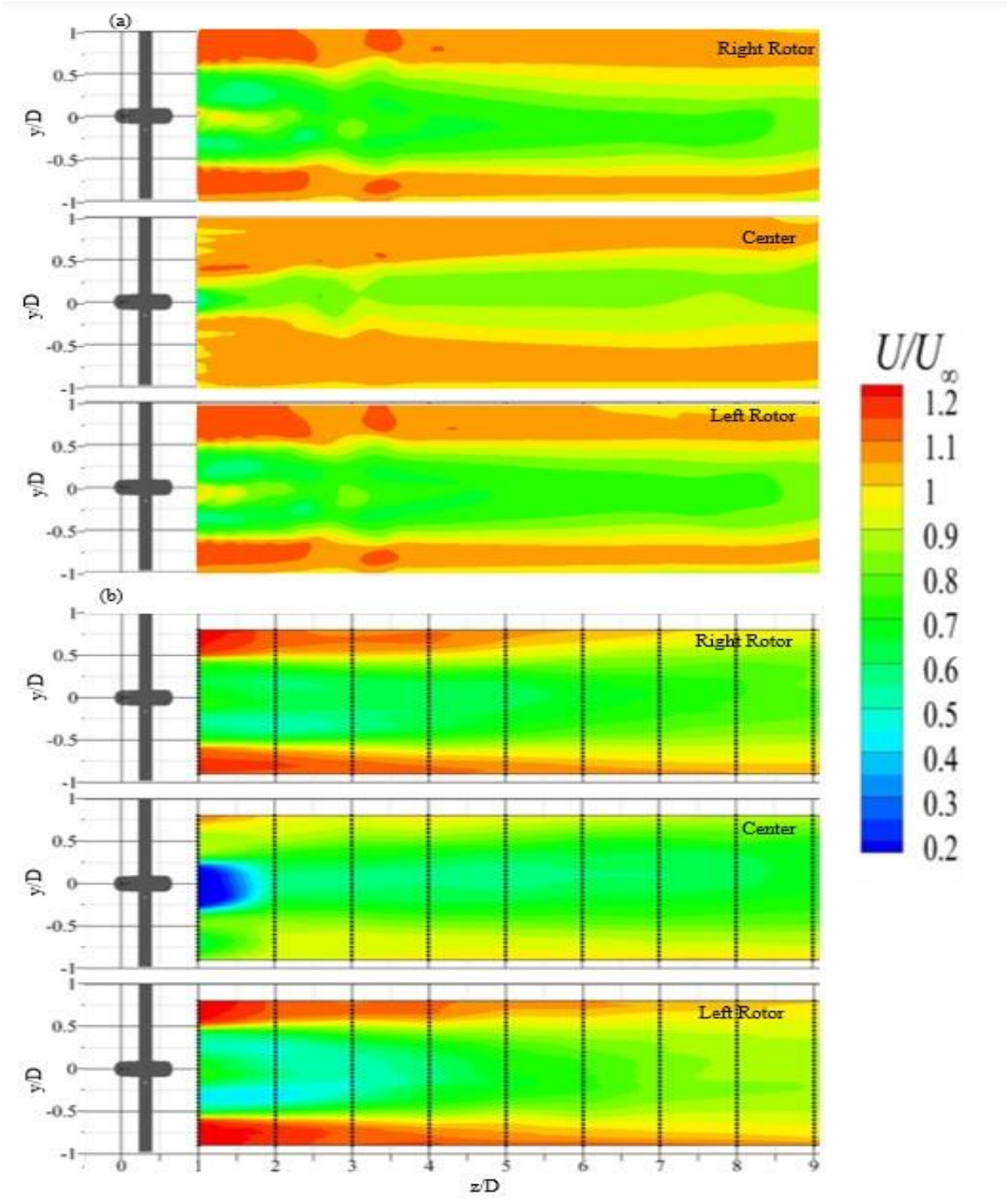

Figure 4.9: Normalized velocity contour in vertical plane downstream of the turbine: (a) simulation (b) experiments [33]. The vertical dotted lines in (b) show actual ADV measurement profile positions

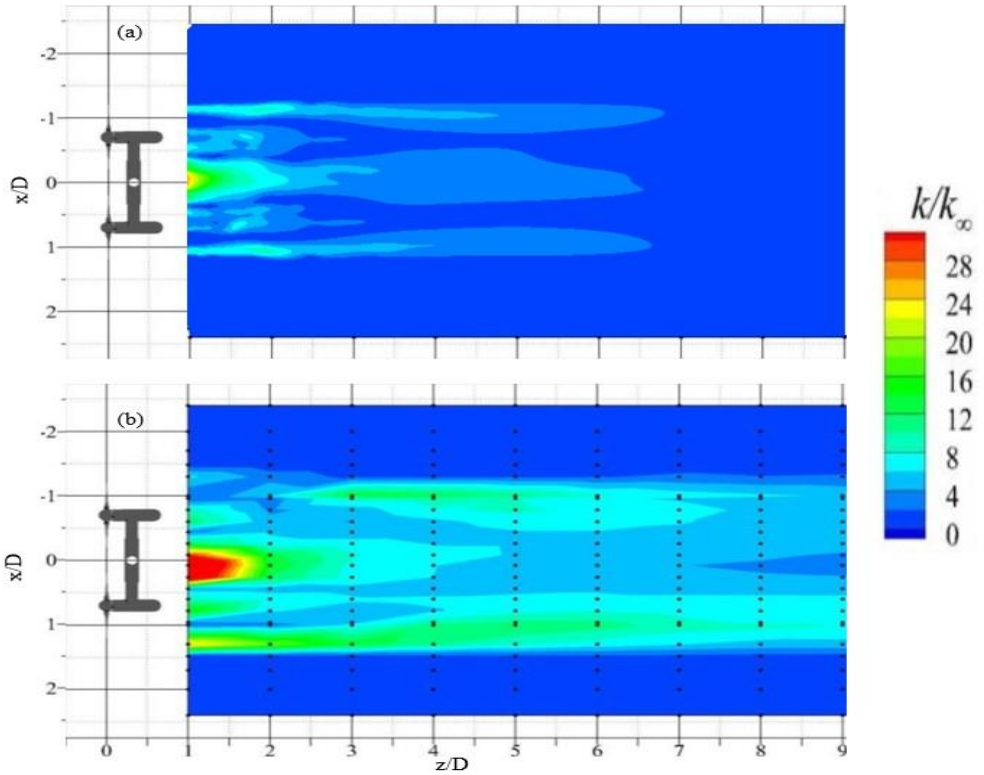

Figure 4.10: Normalized turbulent kinetic energy contours in horizontal plane (y = 0) downstream of the turbine at $\lambda = 5.07$: (a) simulations and (b) experiment [33]. The vertical dotted lines in (b) show actual ADV measurement profile positions.

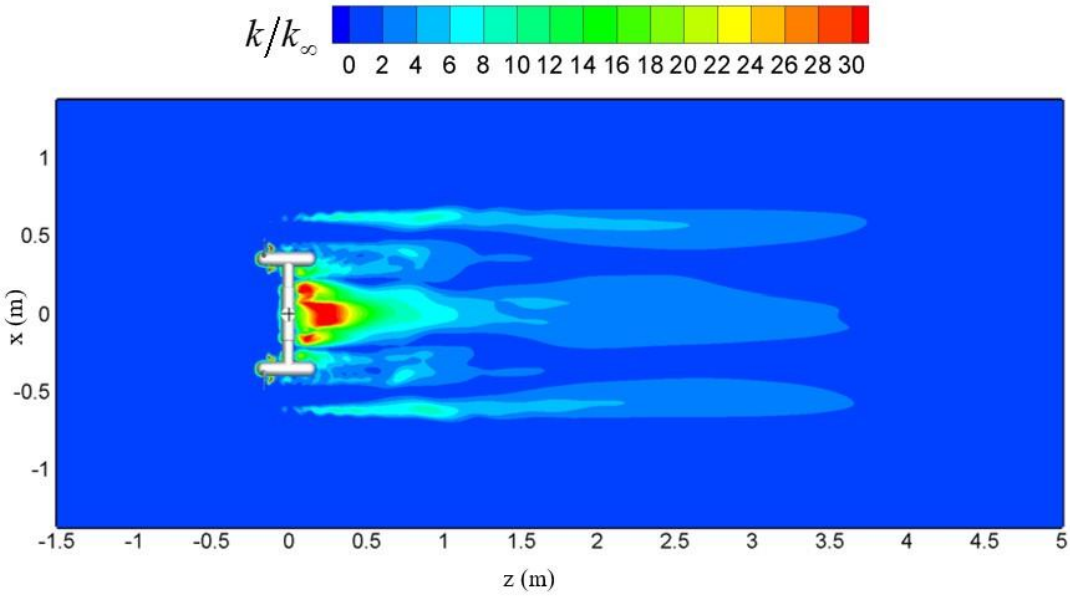

Figure 4.11: Normalized turbulent kinetic energy contour across the domain at mid plane (y = 0) for $\lambda = 5.07$ (simulations)

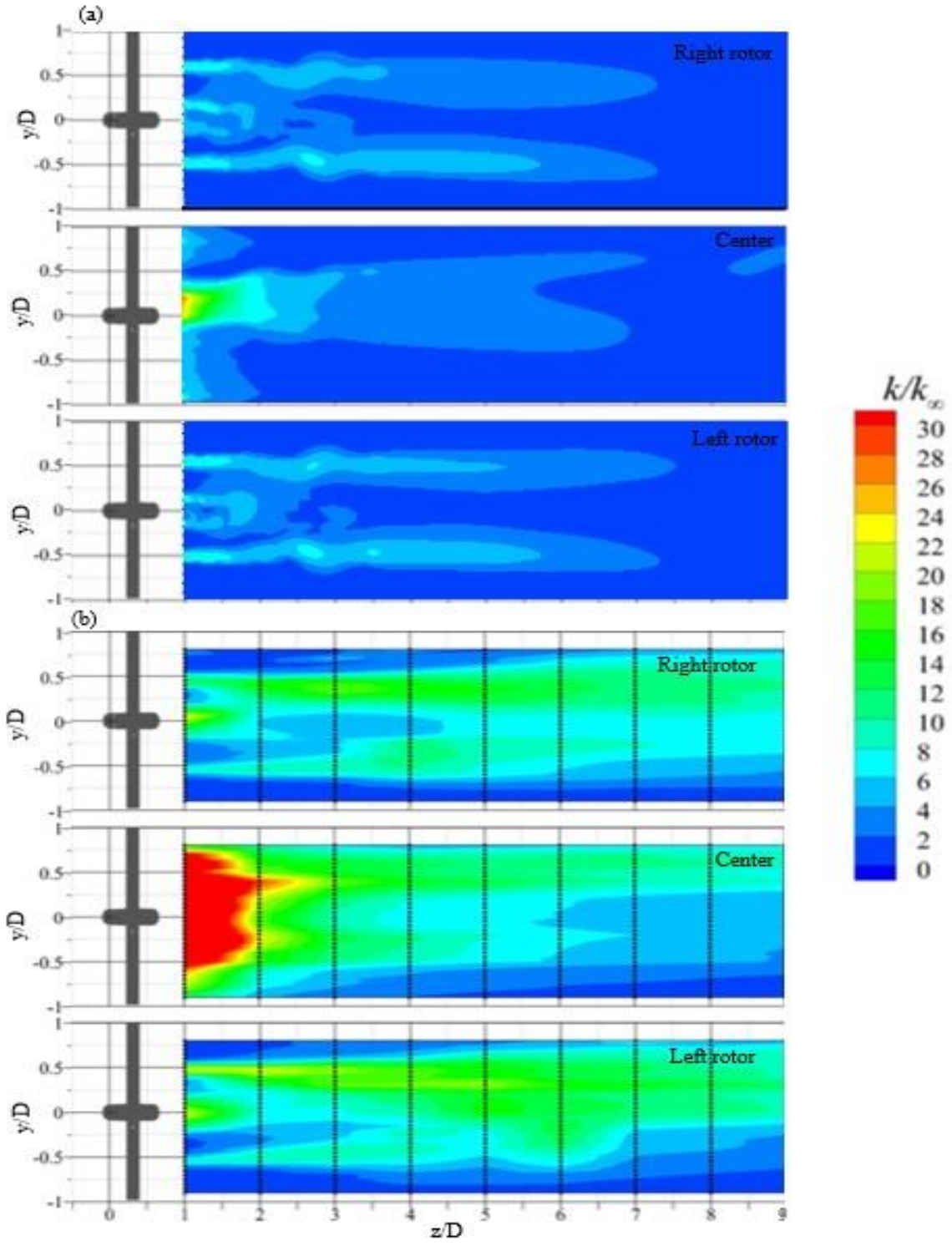

Figure 4.12: Normalized turbulent kinetic energy contour in vertical plane downstream of the turbine: (a) simulation (b) experiments [33]. The vertical dotted lines in (b) show actual ADV measurement profile positions

4.3 WAKE VORTEX STRUCTURES

In order to understand the 3D structure of the wake, vorticity contours are illustrated in Figure 4.13, at different distances in Z and for rotor angular velocities of 90 rpm, 204 rpm and 330 rpm. The vortical structures in the wake are ploted in Figure 4.14 and Figure 4.15, for the same three rotor angular velocities. The plots are iso-surfaces of the streamwise vorticiy calculated using the vorticity indicator Q with a value of 0.05:

$$Q = \frac{1}{2}(S_{ij}S_{ij} - \Omega_{ij}\Omega_{ij}) \tag{4.1}$$

where S_{ij} is mean strain tensor and Ω_{ij} is the vorticity tensor. The contours of the magnitude of velocity are displayed along with iso-surfaces of the vorticity. We know that, as the flow approaches the rotor, pressure rises, and the stream velocity decreases. When the flow passes through the rotor the pressure drastically reduces to its lowest point. As soon as the flow crosses the rotor plane, the velocity and pressure field become non-uniform. This non-uniformity in velocity is related to the vortex structures shed from the blades[41]. We observe two sets of well-organized counter-rotating helicoidal vortex structures arising from each blade in Figure 4.13. The outer wake, dominated by the tip vortices, is rotating in the same direction as the blades, anticlockwise (positive vorticity in red) for the right rotor and clockwise (negative vorticity in blue) for the left rotor. The corresponding inner wake consisting of the root vortices rotates in the direction opposite to the outer wake. This structure is consistent with results obtained by other studies conducted on the wake analysis of a HATT[42]–[44] where for a N-bladed rotor there exist N helical tip vortices and corresponding counter-rotating N root vortices. In our case, the turbine rotors are two bladed, hence each have two sets of tip and root vortices forming a double helix structure in the wake. We also see that the root vortices inner wake frame a region of high velocity at the center, where the turbine hub produces acceleration of the flow, which rotates in the direction opposite to the inner wake, in the region close to the turbines up to around 2D. This phenomenon can be explained by Kelvin's Circulation theorem which states that the circulation around any closed contour in an inviscid flow of a barotropic fluid with conservative body forces does not change with time. If we consider a closed contour around the inner wake, in order to balance out the root vortices, the central core of the wake rotates in the opposite direction with a higher velocity. We also observe a hub vortex generated from the nacelle similar to the structures

observed by Kang et al.[45], where the region between the blades and the nacelle generates a swirling motion in direction opposite to the blade rotation. This causes the hub vortex originating from this region to become unstable resulting in a slowly progressing spiral vortex core as observed in Figure 4.14. This complex system of vortices serves to delineate and constrain the inner wake from the outer wake as they progress downstream. In Figure 4.13 (b) ($\lambda = 5.07$, corresponding angular velocity for the rotors is 204 rpm), as we go downstream to around 4D, we see that the unstable hub vortex has merged with the root vortices and the core of the inner wake rotates as a single wide-core vortex . Up to 4D downstream, we see that the wake is axisymmetric and has an annular structure, but at 4D, the axial symmetry starts to disappear. The outer wake, dominated by the outer tip vortices undergoes an overall radial expansion, caused by the transport of momentum from the higher velocity bypass flow to the wake due to enhanced turbulent mixing and the entrainment of the bottom boundary layer [45]. This signals the onset of pressure recovery in the flow and marks the end of the near wake region and beginning of the transition region [44]. In the transition region, as described by Silva et al. [41], at around 4D - 5D, the process of turbulent mixing is enhanced where the wake interacts with the bypass flow and the tip vortices start to lose their coherency. It is important to note that, in the transition region, the mixing is concentrated around the annular shear layer at the edge of the wake. For our case, due to the delayed mixing in the turbulent closure model, as observed in the velocity deficit plots (Figure 4.4,Figure 4.5Figure 4.6), the transition regions begins at around 4D, and the far wake region that is generally observed around 6D in experiments, starts around 8D from the turbine for our simulations, where the tip vortices start breaking down and we see rapid turbulent mixing.

The 3D vortices produced by the blade and their interactions govern the flow field within the wake and the performance of the turbine. The periodicity of the vortex lines is a function of the circumferential and axial velocity acting on the turbine. These helical vortex lines can be observed in Figure 4.14 and Figure 4.15 which show the iso-surface of vorticity for three tip speed ratios. We see that, for a constant inflow velocity, the distance between the two tip vortex lines in the near wake decreases with increases in angular velocity of the rotor. If we focus on the iso-surfaces for the 204 rpm (optimal λ), we see that at around 2D the vortex lines merge as they are advected downstream in the domain. Due to this merging, TKE is generated, causing the wake to spread out radially, evidence of which can also be seen in Figure 4.8 in the sudden increase in streamwise velocity at that point in the wake. As we go further downstream, the tip vortices slowly start

dissipating and eventually break down. As mentioned earlier, at 6D the inner wake starts merging with the outer wake though the structure is largely intact.

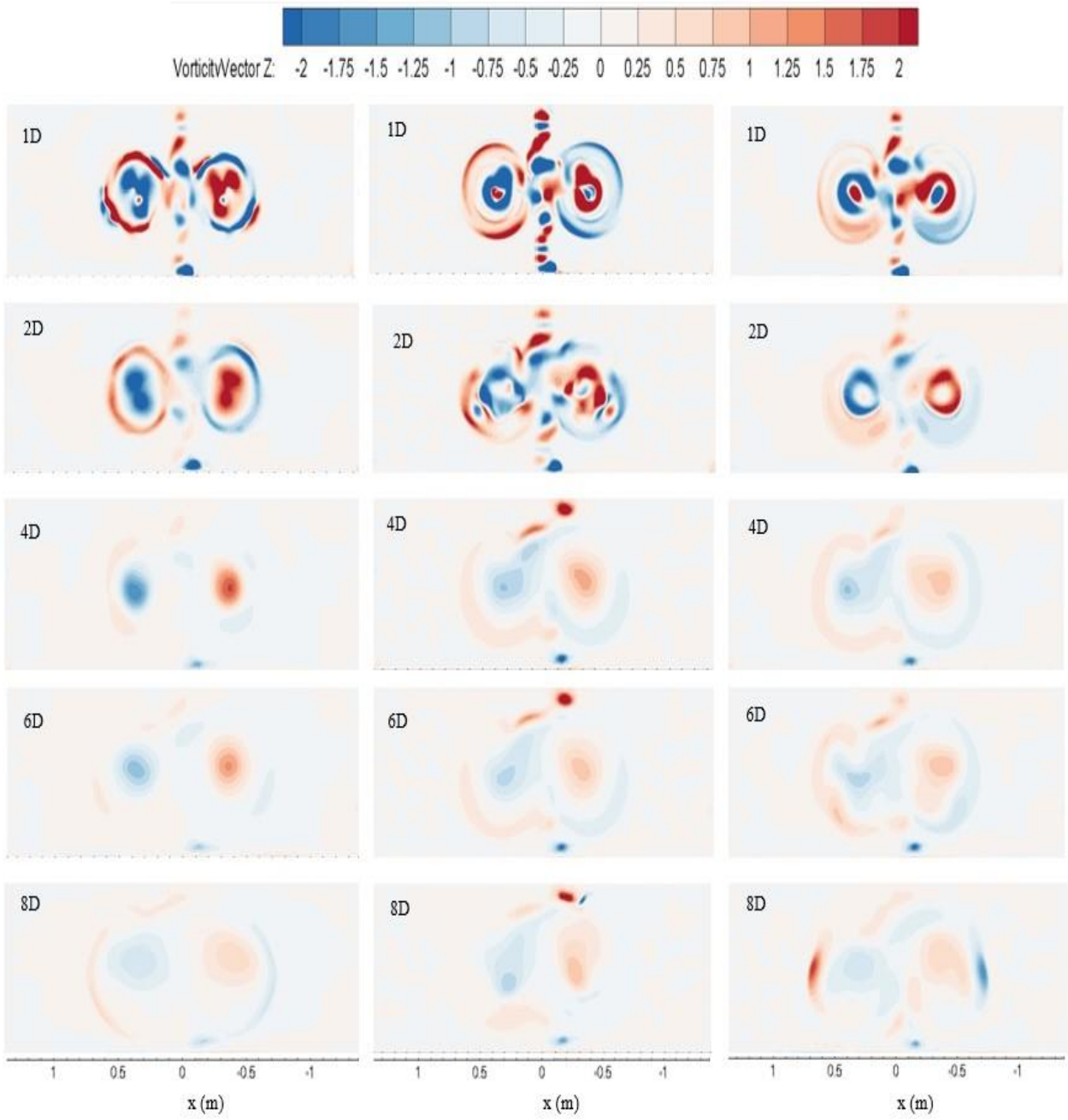

(a) 90 RPM (b) 204 RPM (c) 330 RPM

Figure 4.13: Vorticity contours for three turbine rotation rates (a) 90 rpm, (b) 204 rpm and (c) 330 rpm

At around 8D, the shear layers from the inner wake for both the rotors start moving closer to each other and twist around each other, merging near the end of the computational domain. It is

interesting to observe thick coherent structures surrounding the inner wake towards the end of the domain where ideally the tip vortices are expected to break down and the wake structure is governed by enhanced turbulence mixing (i.e. area beyond 6D downstream). This is unexpected and we suspect that it could a consequence of the wake meandering towards the bottom boundary as documented earlier. Due to the wake expanding close to the bottom wall, the partially coherent vortices that may still exist but are not visualized by the iso-contours could interact with vorticity generated at the walls, thereby causing the vorticity to increase in the wake region, which is captured by the iso-surfaces as thick bands of vorticity merging with the inner wake, as seen in Figure 4.14 (b) and Figure 4.15 (b). The central monopile induces strong von Karman vortices which propagate through the flow in the form of vortex filaments. Since the top boundary is modelled as a symmetry plane, the shear layers from the monopile close to the top boundary do not interact with the other layers. They maintain a constant magnitude of velocity as we move downstream in the domain.

In order to understand these vortex structures better, we recorded the wake behind the turbine for angular velocities of 90 rpm and 330 rpm as seen in Figure 4.14 and Figure 4.15. Consider Figure 4.14 (c) and Figure 4.15(c), which display the wake behind the turbine for 330 rpm: we see that, compared to the optimal case, the tip and root vortices are well-defined but not as regular and strong as at the optimum TSR value. As we mentioned earlier, the pitch of the helical vortices depends on the turbine rotation rates for a given constant freestream velocity. Thus, as a consequence of the higher angular velocity, the tip vortices are closer to each other and have a higher magnitude of velocity. We observe that the combining of adjacent vortices occurs earlier than in the 204-rpm case at 1D downstream of the turbine. This occurs partly due to closer proximity of the tip vortices and partly because for higher λ values the blades have a lower angle of attack. At low angles of attack less lift is generated which corresponds to weaker tip vortices generated. As seen in Figure 4.13 (a), the tip and hub vortices combine at 2D, which is earlier than the optimal case and, as a result, the inner wake expands earlier, and the overall wake expands at faster rate and earlier. The tip vortices lose their shape faster, and twisting, overlapping and merging of the inner vortex for both rotors occurs at 6D instead of at 8D, as result of increase in the rate of rotation. We see that the interaction between the wake and the boundary vortices not only occurs earlier, at around 7D, but the effect is more pronounced as compared to the lower

rotation rate cases. Evidence of this can be seen in Figure 4.13 (c): at 8D, the structures surrounding the wake region have higher levels of vorticity compared to those in Figure 4.13 (b).

For the lowest λ case at 90 rpm, parts of the rotor experience separation, as the blades have a high angle of attack. This causes vortices to shed from the trailing edge. The vorticity iso-surfaces are irregular and the well-defined tip vortices are not observed (see Figure 4.14 and Figure 4.15). The irregularities are due to the interactions between the trailing edge structure in the separated flow and the blade-tip vortices. The overall vortex structure in the near wake is disorganized, which leads to early breakdown and an onset of turbulence mixing. At 4D downstream, we see that the outer wake has started to dissipate and disappears by 6D as seen in Figure 4.13(a). However, unlike in the other cases, the inner vortex core maintains its structure throughout the entire domain, slowly dissipating as we go further downstream. The inner wake for each rotor remains coherent as we go from 1D to 9D. We also observe the interaction of the wake and wall vortices, however, the increase in vorticity is not as pronounced as in the other two cases. It is interesting to note that, for the 90-rpm case, the coherent structures that arise due this peculiar behavior of the wake are thicker and more well-defined. For both the high and low velocity the vortices arising from the central monopile and the horizontal crossarms are not as well-defined, as in the optimal case and disappear quickly, as we move downstream of the turbine.

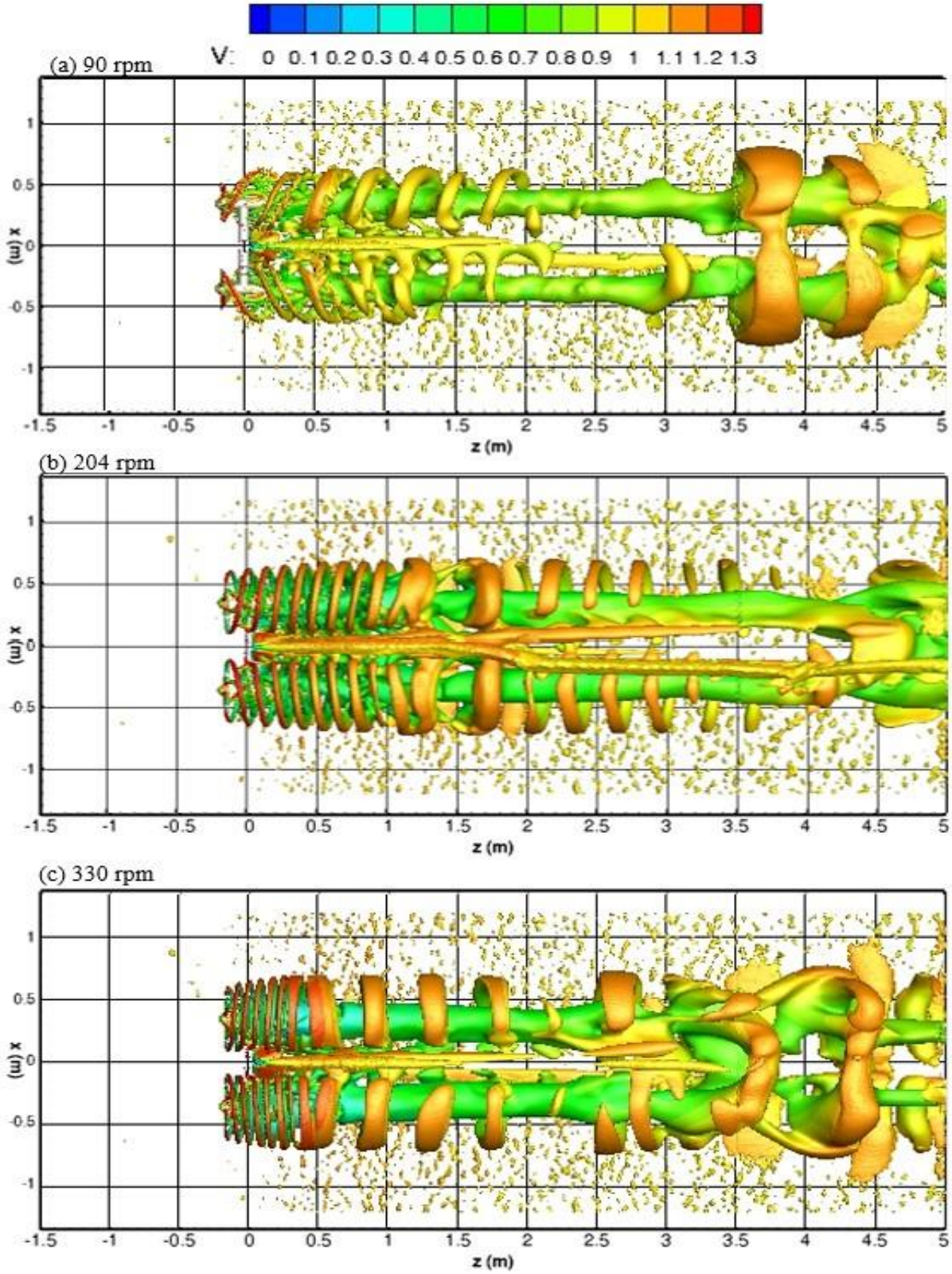

Figure 4.14: Vorticity Iso-surfaces plotted at Q = 0.05 (top view): (a) 204 rpm (b) 90 rpm (c) 330 rpm

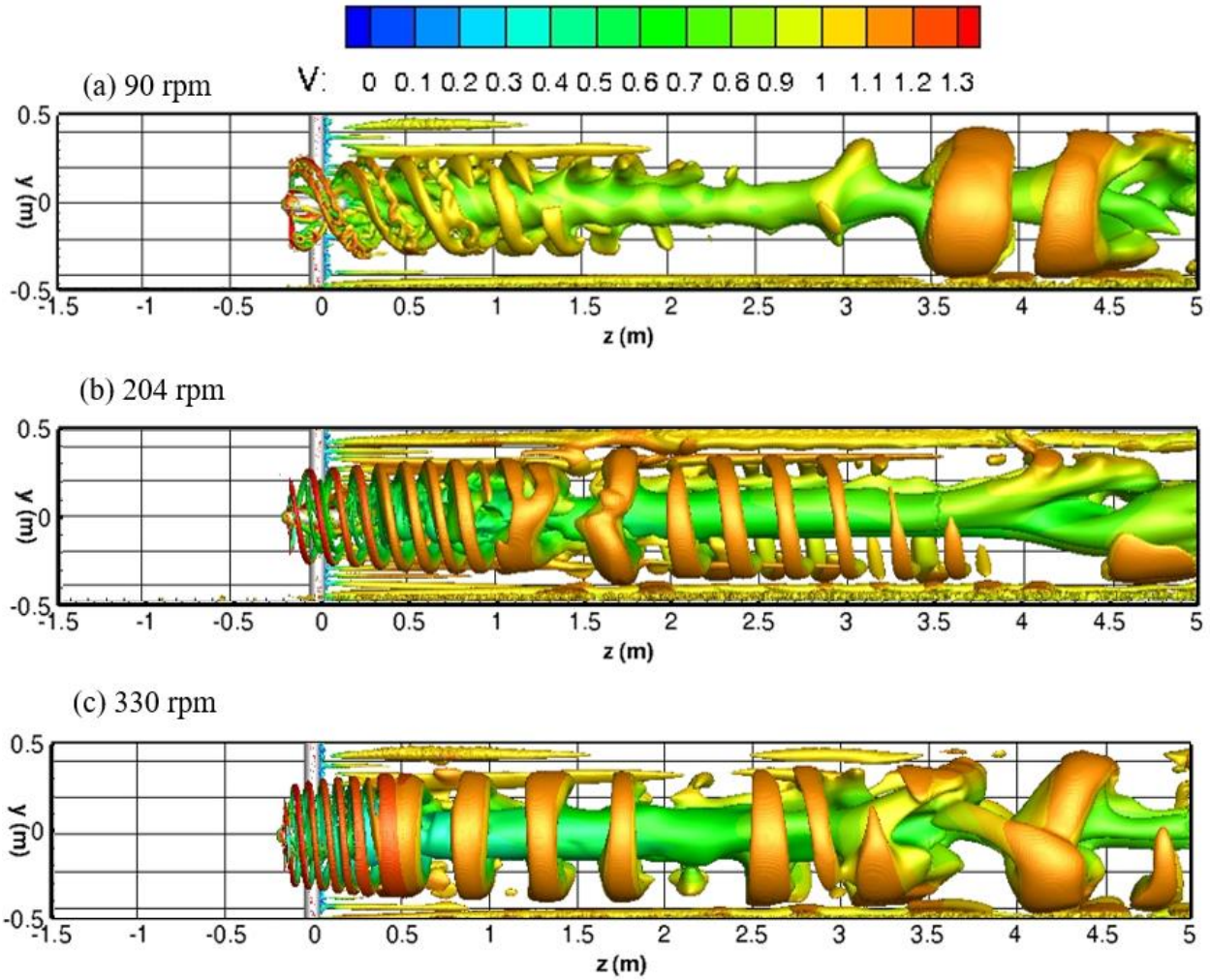

Figure 4.15: Vorticity Iso-surfaces plotted at Q =0.05 (side view) (a) 204 rpm (b) 90 rpm (c)

Chapter 5. CONCLUSIONS AND FUTURE WORK

5.1 CONCLUSION

In this thesis, numerical simulations are performed to conduct a transient analysis of flow over a dual rotor horizontal axis tidal turbine. Results are recorded over a range of tip speed ratios ($\lambda \approx 2$ to 8.32), at a constant upstream velocity of 1.045 m/s . The sliding mesh technique is used to simulate the effect of turbine rotation on the flow, and the RANS realizable $k-\varepsilon$ model is used along with a pressure-velocity coupled solver to cater to the turbulence closure problem. The free surface effects are not taken into consideration, because previous research at UW's NNMREC demonstrated that it is not significant for the conditions studied here [13], [40], and thus is an opportunity to simplify the simulations and save computation costs. The mesh is refined near the blade to capture the boundary layer physics accurately. A refined mesh was used in the wake region to ensure that the wake evolution is also fully captured. A coarse mesh is used in the regions with low gradients, near the inlet, at the sidewalls and the outlet of the domain, in order to minimize number of mesh elements.

The transient results of the turbine performance and the resulting wake are compared with experimental results from the tests performed on this turbine by SAFL at the University of Minnesota, in collaboration with Sandia National Laboratory. It is found that the sliding mesh results can reproduce some important flow characteristics of an actual turbine, for example, tip and root vortex helical structures, as well as steep velocity and turbulent kinetic energy gradients around the turbine blade. In comparison, the numerical results show a good agreement with the experimental measurements in terms of predicted coefficient of performance, velocity in the wake and momentum transferred in the wake. The comparison between experimental measurements and transient simulations results for velocity deficit show that, starting from 4 to 5D, the wake is wider for the simulations. Due to the limitation of the turbulence closure model, as a result of low mesh resolution in the region around the central monopile and horizontal support structures, turbulence properties in that area are underpredicted. As a result of this discrepancy, mixing in this region is inaccurately captured which causes the centerline minima in velocity deficit to exist up to 9D in simulations. Correspondingly, the momentum deficit in this region is also underpredicted for the simulations. Due to the underprediction of the turbulent behavior in the flow, specifically the

phenomenon of delayed mixing, the overall width of the wake in the simulations is affected, increasing the wake recovery distance and reducing recovery rates. The effects of asymmetry in the incoming flow in the experiments cause a variation in power production and flow characteristics between the left and right rotors. This variation is not observed in the simulation results, as the flow complexity and asymmetry are not included due to the used of uniform inlet condition. The comparison of velocity contours show that the simulations can record the overall wake structure very well, consisting of the outer wake region with bordering tip vortices which surrounds the inner wake region made up of the root and hub vortices. We see that the wake remains approximately the of constant width, after initial widening, as the wake travels downstream from the turbine due to the presence of channel walls. The wake is mostly symmetric about the turbine axis, the meandering of the wake towards the free surface due to mixing and momentum transfer is not observed in the simulations in contrast to the experiments, as the free surface is not fully captured by the boundary conditions. Even though the sliding mesh can predict the turbine performance and velocity deficits in the wake in an accurate manner, overall turbulent kinetic energy recorded in the CFD simulations are lower than the experiments. We suspect that this variation is partly due to the k-epsilon model's tendency to overpredict the decay of turbulent kinetic energy and partly due to the sliding mesh model's inability to reproduce separated flow accurately, due to idealized conditions on the rotating reference frame. In order to understand the variation in the wake structures with changing rotor speeds, vortex structures are compared for three tip speed ratios $\lambda = 2.26,5.07,8.32$ at a constant upstream velocity field. Through this comparison we see that each rotor produces two sets of counter-rotating tip and root helical structures. The nacelle creates a hub vortex that quickly combines with the root vortices to form the inner wake region. These structures constrain the wake from the outer bypass flow as the wake moves downstream. The vortices shed by the central cylindrical monopile and horizontal cross-arms are nor well defined and disappear quickly as we move downstream and they merge with the structures produced by the blades. Rapid turbulent mixing is triggered as the inner wake starts merging with the outer wake, which leads to breakdown of the tip vortices. We conclude that the main mechanism affecting the wake recovery in the far wake region is the vortex breakdown, resulting in rapid turbulent mixing. Due to delayed mixing in the simulations, this breakdown happens at a further distance compared to the experiments.

As the rotational speed is increased, we see that the periodicity of the helical structures increases. At the lowest tip speed ratio, we see the iso-structures used to visualize the vortices are irregular due separation of flow from blade stalling. The vortex structures become more defined as the rotor speed increases up to the optimal tip speed ratio where the structures are best defined. Upon further increase of rotor speeds, the tip vortices though still defined, are weaker, and adjacent vortex ropes combine faster. The inner wake for each rotor starts merging earlier with an increase in tip speed ratio, with merging distance from the turbine reducing with increase in speed. At the lowest λ, the wakes are still distinct at the outlet; at the optimal case, they combine towards the end of the domain (around 8D), and at the highest λ, the merging takes place at about 6D. As λ increase, the wake recovery distance increases as the irregularity in the vortex structures decreases. This trend is followed up to the optimal case, after which the recovery distance again reduces due to weaker tip vortices. Interaction between the outer wake structures and the wall vortices is reported for all three cases which causes an unexpected increase in vorticity in the far wake region. It is suspected that this sudden appearance of coherent structures in the far wake region is due to meandering of the wake towards the bottom wall. The increase in vorticity becomes more pronounced as λ increases, but the structures are thick and more well defined for low λ.

The above trends observed give information about the change in wake characteristics like length, width and wake recovery for different turbine operating conditions. These factors play a crucial role in determining turbine array arrangement and designing optimal tidal farms. Despite some limitations associated with predictions of capturing turbulence flow characteristics in RANS simulations, the good qualitative agreement suggests promising results for using the methodology to predict optimum turbine performance and wake structures.

5.2 FUTURE WORK

In this thesis, a numerical methodology has been developed to conduct transient analysis on a HATT. We conclude that the method developed can accurately model the turbine performance and capture the wake structures with a reasonable level of accuracy conmesurate with the computational cost of this RANS simulation. However, the quantitative velocity deficit does not perfectly match the experimental measurements. The model overpredicts the local velocity deficit, overpredicts turbulence kinetic energy decay rate, or underpredicts the TKE production at the

blade surfaces, and shows delayed recovery due to the limitations of the turbulence closure model. For accurate prediction of velocity deficit, the central monopile and horizontal support structures must be resolved, so that the realizable $k-\varepsilon$ model can capture the entirety of flow characteristics. This would, however, increase the overall computational costs of the simulation by a significant amount, x2 to x10 in time and memory requirements, and thus is left to pursue in the future when the resources exist and the need for this type of accuracy is needed in the detailed design of HATT arrays. Thus, for more accurate analysis of the wake either a different closure model like the SST $k-\omega$ model should be used as it does not require the boundary layer to be as finely resolved as the realizable $k-\varepsilon$ model. Even with these limitations, the sliding mesh technique is successful in providing in-depth information about the wake's physical behavior. It is a suitable method for analysis when the transient behavior of wakes is of interest. In this thesis, free surface effects were not considered and a single value of channel blockage is investigated, matching the experiments. It would be interesting to look at the impact that different blockage ratios, including possibly different distances of the turbine rotor to the free surface, have on the turbine performance and transient wake characteristics. Even though the sliding mesh technique provides useful information about the flow around the turbine, it is a computationally expensive and time-consuming technique. Hence it is not yet suitable for analysis of turbine array arrangement. Models like ADM and BEM have proven to predict the far wake characteristics of HATTs accurately, at a comparatively inexpensive manner and, thus, are more suitable for analysis of turbine arrays. The sliding mesh technique can be used to initial in-depth analysis of the wake and turbine design performance followed by an analysis of arrays using the less expensive models.

BIBLIOGRAPHY

[1] "Energy policy: general principles | Fact Sheets on the European Union | European Parliament." [Online]. Available: http://www.europarl.europa.eu/factsheets/en/sheet/68/energy-policy-general-principles.

[2] "A Guide to Initiative 937." [Online]. Available: https://www.washingtonpolicy.org/publications/detail/a-guide-to-initiative-937.

[3] A. T. J. Mozafari, "Numerical Modeling of Tidal Turbines: Methodology Development and Potential Physical Environmental Effects," p. 158.

[4] T. J. Hall, "Numerical Simulation of a Cross Flow Marine Hydrokinetic Turbine," p. 105.

[5] "Quarter moon, Earth perihelion, neap tide | Science Wire | EarthSky." [Online]. Available: https://earthsky.org/space/quarter-moon-earth-at-perihelion-and-neap-tide.

[6] A. Roberts, B. Thomas, P. Sewell, Z. Khan, S. Balmain, and J. Gillman, "Current tidal power technologies and their suitability for applications in coastal and marine areas," *J. Ocean Eng. Mar. Energy*, vol. 2, no. 2, pp. 227–245, May 2016.

[7] C. H. Lebarbier, "Power from Tides— the Rance Tidal Power Station," *Naval Engineers Journal*, vol. 87, no. 2, pp. 57–71, 1975.

[8] I. Fairley, R. Ahmadian, R. A. Falconer, M. R. Willis, and I. Masters, "The effects of a Severn Barrage on wave conditions in the Bristol Channel," *Renewable Energy*, vol. 68, pp. 428–442, Aug. 2014.

[9] L. E. Myers and A. S. Bahaj, "Experimental analysis of the flow field around horizontal axis tidal turbines by use of scale mesh disk rotor simulators," *Ocean Engineering*, vol. 37, no. 2–3, pp. 218–227, Feb. 2010.

[10] T. Burton, Ed., *Wind energy: handbook*. Chichester ; New York: J. Wiley, 2001.

[11] C. Garrett and P. Cummins, "The efficiency of a turbine in a tidal channel," *J. Fluid Mech.*, vol. 588, pp. 243–251, Oct. 2007.

[12] B. L. Polagye, "Hydrodynamic Effects of Kinetic Power Extraction by In-Stream Tidal Turbines," p. 206.

[13] S. J. Adamski, "Numerical Modeling of the Effects of a Free Surface on the Operating Characteristics of Marine Hydrokinetic Turbines," p. 157.

[14] M. J. Khan, G. Bhuyan, M. T. Iqbal, and J. E. Quaicoe, "Hydrokinetic energy conversion systems and assessment of horizontal and vertical axis turbines for river and tidal applications: A technology status review," *Applied Energy*, vol. 86, no. 10, pp. 1823–1835, Oct. 2009.

[15] L. Battisti, A. Brighenti, E. Benini, and M. R. Castelli, “Analysis of Different Blade Architectures on small VAWT Performance,” *J. Phys.: Conf. Ser.*, vol. 753, p. 062009, Sep. 2016.

[16] A. S. Bahaj, A. F. Molland, J. R. Chaplin, and W. M. J. Batten, “Power and thrust measurements of marine current turbines under various hydrodynamic flow conditions in a cavitation tunnel and a towing tank,” *Renewable Energy*, vol. 32, no. 3, pp. 407–426, Mar. 2007.

[17] M. E. Harrison, W. M. J. Batten, L. E. Myers, and A. S. Bahaj, “Comparison between CFD simulations and experiments for predicting the far wake of horizontal axis tidal turbines,” *IET Renew. Power Gener.*, vol. 4, no. 6, p. 613, 2010.

[18] A. S. Bahaj, W. M. J. Batten, and G. McCann, “Experimental verifications of numerical predictions for the hydrodynamic performance of horizontal axis marine current turbines,” *Renewable Energy*, vol. 32, no. 15, pp. 2479–2490, Dec. 2007.

[19] S. R. Turnock, A. B. Phillips, J. Banks, and R. Nicholls-Lee, “Modelling tidal current turbine wakes using a coupled RANS-BEMT approach as a tool for analysing power capture of arrays of turbines,” *Ocean Engineering*, vol. 38, no. 11–12, pp. 1300–1307, Aug. 2011.

[20] W. M. J. Batten, A. S. Bahaj, A. F. Molland, and J. R. Chaplin, “Experimentally validated numerical method for the hydrodynamic design of horizontal axis tidal turbines,” *Ocean Engineering*, vol. 34, no. 7, pp. 1013–1020, May 2007.

[21] R. Malki, A. J. Williams, T. N. Croft, M. Togneri, and I. Masters, “A coupled blade element momentum – Computational fluid dynamics model for evaluating tidal stream turbine performance,” *Applied Mathematical Modelling*, vol. 37, no. 5, pp. 3006–3020, Mar. 2013.

[22] J. Liu, H. Lin, and S. R. Purimitla, “Wake field studies of tidal current turbines with different numerical methods,” *Ocean Engineering*, vol. 117, pp. 383–397, May 2016.

[23] T. Javaherchi, N. Stelzenmuller, J. Seydel, and A. Aliseda, “EXPERIMENTAL AND NUMERICAL ANALYSIS OF A SCALE-MODEL HORIZONTAL AXIS HYDROKINETIC TURBINE,” p. 10.

[24] Y. Sun and L. Zhang, “Numerical Simulation of the Unsteady Flow and Power of Horizontal Axis Wind Turbine using Sliding Mesh,” in *2010 Asia-Pacific Power and Energy Engineering Conference*, 2010, pp. 1–3.

[25] J. McNaughton, I. Afgan, D. D. Apsley, S. Rolfo, T. Stallard, and P. K. Stansby, “A simple sliding-mesh interface procedure and its application to the CFD simulation of a tidal-stream turbine: SLIDING-MESH INTERFACE FOR CFD SIMULATION OF A TIDAL-STREAM TURBINE,” *International Journal for Numerical Methods in Fluids*, vol. 74, no. 4, pp. 250–269, Feb. 2014.

[26] I. Afgan, J. McNaughton, S. Rolfo, D. D. Apsley, T. Stallard, and P. Stansby, “Turbulent flow and loading on a tidal stream turbine by LES and RANS,” *International Journal of Heat and Fluid Flow*, vol. 43, pp. 96–108, Oct. 2013.

[27] T. Leroux, N. Osbourne, J. M. McMillan, D. Groulx, and A. E. Hay, “Numerical Modelling of a Tidal Turbine Behaviour under Realistic Unsteady Tidal Flow,” p. 11.

[28] T. Leroux, N. Osbourne, and D. Groulx, “Numerical study into horizontal tidal turbine wake velocity deficit: Quasi-steady state and transient approaches,” *Ocean Engineering*, vol. 181, pp. 240–251, Jun. 2019.

[29] F. R. Menter, “Two-equation eddy-viscosity turbulence models for engineering applications,” *AIAA Journal*, vol. 32, no. 8, pp. 1598–1605, Aug. 1994.

[30] W. M. J. Batten, M. E. Harrison, and A. S. Bahaj, “Accuracy of the actuator disc-RANS approach for predicting the performance and wake of tidal turbines,” *Proc. R. Soc. A*, vol. 371, no. 1985, p. 20120293, Feb. 2013.

[31] A. Makridis and J. Chick, “CFD Modeling of the wake interactions of two wind turbines on a Gaussian hill,” p. 9.

[32] W. P. Jones and B. E. Launder, “The prediction of laminarization with a two-equation model of turbulence,” *International Journal of Heat and Mass Transfer*, vol. 15, no. 2, pp. 301–314, Feb. 1972.

[33] Tsan-Hsing Shih, William W. Liou, Aamir Shabbir, Zhigang Yang,Jiang Zhu, “A new k-ϵ eddy viscosity model for high reynolds number turbulent flows, Computers & Fluids,” *Computers Fluids*, vol. 24, no. No. 3, pp. 227–238, 1995.

[34] W. RODI, “Experience with two-layer models combining the k-epsilon model with a one-equation model near the wall,” in *29th Aerospace Sciences Meeting*, 0 vols., American Institute of Aeronautics and Astronautics, 1991.

[35] “Theory.” [Online].STAR CCM+ Users Manual. http://www.cd-adapco.com/products/star-ccm/documentation .

[36] S. M. Salim and S. C. Cheah, “Wall y+ Strategy for Dealing with Wall-bounded Turbulent Flows,” *Hong Kong*, p. 6, 2009.

[37] “Turbulent flows (Stephen B. Pope) .pdf.” .

[38] “Wall Treatment.” [Online].STAR CCM+ Users Manual. http://www.cd-adapco.com/products/star-ccm/documentation .

[39] C. Hill, V. S. Neary, B. Gunawan, M. Guala, and F. Sotiropoulos, “U.S. Department of Energy Reference Model Program RM1: Experimental Results,” p. 28.

[40] S. Adamski and A. Aliseda, “Numerical modeling of the effects of a free surface on the operating characteristics of Marine Hydrokinetic Turbines,” *Bulletin of the American Physical Society,* vol. 57, 2012.

[41] P. A. S. F. Silva, T. F. D. Oliveira, A. C. P. Brasil Junior, and J. R. P. Vaz, “Numerical Study of Wake Characteristics in a Horizontal-Axis Hydrokinetic Turbine,” *An. Acad. Bras. Ciênc.*, vol. 88, no. 4, pp. 2441–2456, Dec. 2016.

[42] C. Daskiran, J. Riglin, W. Schleicher, and A. Oztekin, “Transient analysis of micro-hydrokinetic turbines for river applications,” *Ocean Engineering*, vol. 129, pp. 291–300, Jan. 2017.

[43] T. Stallard, R. Collings, T. Feng, and J. Whelan, “Interactions between tidal turbine wakes: experimental study of a group of three-bladed rotors,” *Proc. R. Soc. A*, vol. 371, no. 1985, p. 20120159, Feb. 2013.

[44] M. Boudreau and G. Dumas, “Vortex Dynamics in the Wake of Three Generic Types of Freestream Turbines,” *Journal of Fluids Engineering*, vol. 140, no. 2, p. 021106, Feb. 2018.

[45] S. Kang, X. Yang, and F. Sotiropoulos, “On the onset of wake meandering for an axial flow turbine in a turbulent open channel flow,” *J. Fluid Mech.*, vol. 744, pp. 376–403, Apr. 2014.